

# Thermal response analysis of multi-layered magneto-electro-thermo-elastic plates using higher order shear deformation theory

M. Vinyas<sup>\*1</sup>, D. Harursampath<sup>1</sup> and S.C. Kattimani<sup>2</sup>

<sup>1</sup>Non-linear Multifunctional Composites Analysis and Design (NMCAD) Lab, Department of Aerospace Engineering, Indian Institute of Science, Bangalore, 560012, India

<sup>2</sup>Department of Mechanical Engineering, National Institute of Technology Karnataka, Surathkal, 575025, India

(Received April 25, 2019, Revised October 15, 2019, Accepted November 12, 2019)

**Abstract.** In this article, the static responses of layered magneto-electro-thermo-elastic (METE) plates in thermal environment have been investigated through FE methods. By using Reddy's third order shear deformation theory (TSDT) in association with the Hamilton's principle, the direct and derived quantities of the coupled system have been obtained. The coupled governing equations of METE plates have been derived through condensation technique. Three layered METE plates composed of piezoelectric and piezomagnetic phases are considered for evaluation. For investigating the correctness and accuracy, the results in this article are validated with previous researches. In addition, a special attention has been paid to evaluate the influence of different electro-magnetic boundary conditions and pyrocoupling on the coupled response of METE plates. Finally, the influence of stacking sequences, magnitude of temperature load and aspect ratio on the coupled static response of METE plates are investigated in detail.

**Keywords:** Reddy's third order shear deformation theory; magneto-electro-elastic; temperature loading; pyrocoupling; open and closed circuit; static quantities

## 1. Introduction

In the engineering domain, recent technologies have paved way for the extensive utilisation of multifunctional structures. These structures are fundamentally designed by adopting various smart materials. Among them, magneto-electro-elastic (MEE) materials have received a significant attention due to their energy transforming capabilities. These unique form of materials are the combination of piezoelectric and piezomagnetic phases. The potential applications of these materials can be witnessed in stability control, sensors, actuators and energy harvesting etc. A comprehensive analysis on the MEE structures was performed by numerous researchers due to their beneficial coupling properties. For the first time, Pan (2001a) analysed the frequency characteristics of MEE plate through exact solutions. Based on the different layer-wise models the natural frequency characteristics of MEE structures were evaluated by Milazzo (2013). Later, many prominent computational techniques such as state vector approach (Xin *et al.* 2015, Wang *et al.* 2003, Chen *et al.* 2007), approximate solution method (Huang *et al.* 2007), finite element (FE) methods (Vinyas and Kattimani 2018a), mesh less method (Sladek *et al.* 2013) were put forward by various researchers to demonstrate the frequency response of MEE plates.

The static behaviour of MEE plates subjected to different mechanical loading conditions has been dealt by

many researchers. Among them, Pan (2001b) evaluated the static parameters of MEE plates subjected to surface and internal loading through exact solutions. Pan and Han (2005) extended the similar studies to assess the structural behaviour of functionally graded magneto-electro-elastic (FGMEE) plates. The influence of stacking sequences on the static performance of multi-layered MEE plates subjected to magnetic, electric and mechanical loads were investigated by Pan and Heyliger (2003). With the aid of FE methods, Lage *et al.* (2004) studied the coupled response of MEE plates. Moita *et al.* (2009) analysed the static parameters using higher order FE methods. Using analytical and semi-analytical techniques Huang *et al.* (2010) evaluated the static behaviour of FGMEE beam. Also, other prominent literatures considering equivalent single layer and layer-wise models have been reported on assessing the static behaviour of MEE multilayered structures (Alaimo *et al.* 2014, Milazzo 2013, 2014a, b, Benedetti *et al.* 2017). Also, the nonlinear free vibration analysis was performed by Razavi and Shooshtari (2015). Shooshtari and Razavi (2015a, b) also extended their evaluation to assess the effect of elastic medium on the large amplitude free vibrations of MEE plate and shells.

By the virtue of increased demand of smart materials, the analysis of intelligent structures made of these smart materials have been a great interest (Chen *et al.* 2001, Saadatfar *et al.* 2015, Kerur *et al.* 2013, Altay *et al.* 2000). The MEE structures in thermal environment exhibit a completely indifferent behaviour in contrast to the mechanical loading. In addition, the characteristics behaviour of MEE materials, linear constitutive equations, and thus the equations of motion for METE material alter

\*Corresponding author, Ph.D.

E-mail: [vinyasmahesh@iisc.ac.in](mailto:vinyasmahesh@iisc.ac.in), [vinyas.mahesh@gmail.com](mailto:vinyas.mahesh@gmail.com)

tremendously (Sunar *et al.* 2002). In this regard, many researchers have attempted to investigate the thermal effects on the structural response of MEE plates, beams and shells. Among them, Kumaravel *et al.* (2007) evaluated the static response of MEE beam using FE methods. The effects of pyrocoupling on the static parameters of MEE structures were investigated by Kondaiah *et al.* (2012, 2013a, b). Vinyas and Kattimani (2017a, b, c, d, e, f) proposed a unique FE formulation on the basis of total potential energy principle, to study the effect of various thermal loading on the layered as well as stepped-functionally graded MEE (SFG-MEE) plates and beams. Also, Vinyas and Kattimani (2017g, 2018b) extended their evaluation to assess the effect of moisture as well. Meanwhile, the topological effects of the MEE material on the coupled structural response was investigated by Vinyas and Kattimani (2018c) and Vinyas *et al.* (2018). Vinyas *et al.* (2017g) investigated the static behaviour of SFG-MEE plate subjected to various combined loading such as mechanical, thermal, electrical and magnetic loads, with the aid of first order shear deformation theory (FSDT). Adopting FSDT, Badri and Kayiem (2013) analysed the static and dynamic analysis of METE plates. Nevertheless, transverse shear strain in the FSDT is constant through the thickness of the MEE plate. Therefore, in order to adjust the transverse shear stiffness, FSDT demands an additional shear correction factor (Ebrahimi and Shafiei 2017). Also, the proper selection of shear correction factors depends on the material properties and the geometrical conditions. Hence, the accuracy of the FSDT strongly depends on the shear correction factors (Ebrahimi and Shafiei 2017, Vinyas 2019). To encounter this drawback and to satisfy zero traction boundary condition, Reddy's third order shear deformation theory is found to be suitable. Further, through employing TSDT, The kinematics of the structure can be represented in a better way. In hygrothermal environment, the ability of HSDT to consider coupling effects to evaluate the natural frequencies was thoroughly investigated by Vinyas and Kattimani (2018b), Vinyas *et al.* (2019a, b, c, d). In addition, the influence of carbon nano-tubes (CNT) on the frequency response of MEE plates with the aid of HSDT was assessed through a FE formulation by Vinyas (2019a). The rectangular/square plates when provided with skewed edges, the stiffness drastically increases due to the fact that the area decreases. This improves the frequency of the plate. In addition, skewed MEE structures can be aligned easily even in case of obstructions. Therefore, the skewed structures are more often seen in the applications such as and actuators, energy harvesting and active vibration control (Vinyas 2019b, Vinyas and Kattimani 2019). The free vibration behaviour of skew MEE plate was discussed by Vinyas *et al.* (2019a, b) through higher-order shear deformation theory.

The exhaustive literature survey reveals that the article reported on thermal analysis of METE structures are available in scarce. Further, to the best of authors' knowledge, no work has been reported on FE study of METE plates under the framework of TSDT considering different electro-magnetic boundary conditions. Even though, the authors' own work on stepped functionally

graded magneto-electro-elastic reveals significant details on the thermal analysis of the METE plates, it does not satisfies the zero shear stress condition on the top and bottom surfaces. This motivated the authors to exploit the benefits of TSDT, METE coupling and FE methods altogether to study the structural behaviour of METE plates. In this regard, this article makes the first attempt towards assessing the multiphysics response of METE plates. Parametric studies are also performed to investigate the effects of stacking sequences, electro-magnetic boundary conditions, pyrocoupling and aspect ratio.

## 2. Material properties and methods

Considering the coupling between elastic, electric, magnetic and thermal fields the coupled constitutive equations of METE materials can be expressed as follows (Kondaiah *et al.* 2013a)

$$\{\sigma^n\} = [C^n]\{\varepsilon^n\} - [e^n]\{E^n\} - [q^n]\{H^n\} - [\alpha^n]\Delta T \quad (1)$$

$$\{D^n\} = [e^n]^T\{\varepsilon^n\} + [\eta^n]\{E^n\} + [m^n]\{H^n\} + [p^n]\Delta T \quad (2)$$

$$\{B^n\} = [q^n]^T\{\varepsilon^n\} + [m^n]\{E^n\} + [\mu^n]\{H^n\} + [\lambda^n]\Delta T \quad (3)$$

The various material properties appearing in Eqs. (1)-(3) are illustrated in Appendix-A. Further,  $n$  and  $\Delta T$  represents the layer number and temperature gradient, respectively.

Meanwhile, Eqs. (1)-(3) can be expressed as follows (Ansari and Gholami 2016, Gholami *et al.* 2017)

$$\begin{aligned} \begin{Bmatrix} \sigma_x \\ \sigma_y \\ \tau_{xy} \\ \tau_{xz} \\ \tau_{yz} \end{Bmatrix} &= \begin{bmatrix} \tilde{C}_{11} & \tilde{C}_{12} & 0 & 0 & 0 \\ \tilde{C}_{12} & \tilde{C}_{22} & 0 & 0 & 0 \\ 0 & 0 & \tilde{C}_{66} & 0 & 0 \\ 0 & 0 & 0 & \tilde{C}_{55} & 0 \\ 0 & 0 & 0 & 0 & \tilde{C}_{44} \end{bmatrix} \begin{Bmatrix} \varepsilon_x \\ \varepsilon_y \\ \gamma_{xy} \\ \gamma_{xz} \\ \gamma_{yz} \end{Bmatrix} \\ &- \begin{bmatrix} 0 & 0 & \tilde{e}_{31} \\ 0 & 0 & \tilde{e}_{32} \\ 0 & 0 & 0 \\ \tilde{e}_{15} & 0 & 0 \\ 0 & \tilde{e}_{24} & 0 \end{bmatrix} \begin{Bmatrix} E_x \\ E_y \\ E_z \end{Bmatrix} - \begin{bmatrix} 0 & 0 & \tilde{q}_{31} \\ 0 & 0 & \tilde{q}_{32} \\ 0 & 0 & 0 \\ \tilde{q}_{15} & 0 & 0 \\ 0 & \tilde{q}_{24} & 0 \end{bmatrix} \begin{Bmatrix} H_x \\ H_y \\ H_z \end{Bmatrix} \\ &- [C_b] \begin{bmatrix} \tilde{\alpha}_1 \\ \tilde{\alpha}_2 \\ 0 \\ 0 \end{bmatrix} \Delta T \\ \begin{Bmatrix} D_x \\ D_y \\ D_z \end{Bmatrix} &= \begin{bmatrix} 0 & 0 & \tilde{e}_{31} \\ 0 & 0 & \tilde{e}_{32} \\ 0 & 0 & 0 \\ \tilde{e}_{15} & 0 & 0 \\ 0 & \tilde{e}_{24} & 0 \end{bmatrix}^T \begin{Bmatrix} \varepsilon_x \\ \varepsilon_y \\ \gamma_{xy} \\ \gamma_{xz} \\ \gamma_{yz} \end{Bmatrix} \\ &+ \begin{bmatrix} \tilde{\eta}_{11} & 0 & 0 \\ 0 & \tilde{\eta}_{22} & 0 \\ 0 & 0 & \tilde{\eta}_{33} \end{bmatrix} \begin{Bmatrix} E_x \\ E_y \\ E_z \end{Bmatrix} + \begin{bmatrix} \tilde{m}_{11} & 0 & 0 \\ 0 & \tilde{m}_{22} & 0 \\ 0 & 0 & \tilde{m}_{33} \end{bmatrix} \begin{Bmatrix} H_x \\ H_y \\ H_z \end{Bmatrix} \\ &+ \begin{bmatrix} \tilde{p}_1 \\ \tilde{p}_2 \\ \tilde{p}_3 \end{bmatrix} \Delta T \end{aligned} \quad (4)$$

$$\begin{aligned} \begin{Bmatrix} D_x \\ D_y \\ D_z \end{Bmatrix} &= \begin{bmatrix} 0 & 0 & \tilde{e}_{31} \\ 0 & 0 & \tilde{e}_{32} \\ 0 & 0 & 0 \\ \tilde{e}_{15} & 0 & 0 \\ 0 & \tilde{e}_{24} & 0 \end{bmatrix}^T \begin{Bmatrix} \varepsilon_x \\ \varepsilon_y \\ \gamma_{xy} \\ \gamma_{xz} \\ \gamma_{yz} \end{Bmatrix} \\ &+ \begin{bmatrix} \tilde{\eta}_{11} & 0 & 0 \\ 0 & \tilde{\eta}_{22} & 0 \\ 0 & 0 & \tilde{\eta}_{33} \end{bmatrix} \begin{Bmatrix} E_x \\ E_y \\ E_z \end{Bmatrix} + \begin{bmatrix} \tilde{m}_{11} & 0 & 0 \\ 0 & \tilde{m}_{22} & 0 \\ 0 & 0 & \tilde{m}_{33} \end{bmatrix} \begin{Bmatrix} H_x \\ H_y \\ H_z \end{Bmatrix} \\ &+ \begin{bmatrix} \tilde{p}_1 \\ \tilde{p}_2 \\ \tilde{p}_3 \end{bmatrix} \Delta T \end{aligned} \quad (5)$$

$$\begin{aligned}
\begin{Bmatrix} B_x \\ B_y \\ B_z \end{Bmatrix} &= \begin{bmatrix} 0 & 0 & \tilde{q}_{31} \\ 0 & 0 & \tilde{q}_{32} \\ \tilde{q}_{15} & 0 & 0 \\ 0 & \tilde{q}_{24} & 0 \end{bmatrix}^T \begin{Bmatrix} \epsilon_x \\ \epsilon_y \\ \gamma_{xy} \\ \gamma_{xz} \\ \gamma_{yz} \end{Bmatrix} \\
&+ \begin{bmatrix} \tilde{m}_{11} & 0 & 0 \\ 0 & \tilde{m}_{22} & 0 \\ 0 & 0 & \tilde{m}_{33} \end{bmatrix} \begin{Bmatrix} E_x \\ E_y \\ E_z \end{Bmatrix} + \begin{bmatrix} \tilde{\mu}_{11} & 0 & 0 \\ 0 & \tilde{\mu}_{22} & 0 \\ 0 & 0 & \tilde{\mu}_{33} \end{bmatrix} \begin{Bmatrix} H_x \\ H_y \\ H_z \end{Bmatrix} \quad (6) \\
&+ \begin{bmatrix} \tilde{\lambda}_1 \\ \tilde{\lambda}_2 \\ \tilde{\lambda}_3 \end{bmatrix} \Delta T
\end{aligned}$$

For the sake of simplicity, the material properties have been split into bending and shear material constants as follows

$$\begin{aligned}
[C_b] &= \begin{bmatrix} \tilde{C}_{11} & \tilde{C}_{12} & 0 \\ \tilde{C}_{12} & \tilde{C}_{22} & 0 \\ 0 & 0 & \tilde{C}_{66} \end{bmatrix}; [C_s] = \begin{bmatrix} \tilde{C}_{55} & 0 \\ 0 & \tilde{C}_{44} \end{bmatrix}; \\
[e_b] &= \begin{bmatrix} 0 & 0 & \tilde{e}_{31} \\ 0 & 0 & \tilde{e}_{32} \\ 0 & 0 & 0 \end{bmatrix}^T; [e_s] = \begin{bmatrix} \tilde{e}_{15} & 0 & 0 \\ 0 & \tilde{e}_{24} & 0 \end{bmatrix}^T; \\
[\mu] &= \begin{bmatrix} \tilde{\mu}_{11} & 0 & 0 \\ 0 & \tilde{\mu}_{22} & 0 \\ 0 & 0 & \tilde{\mu}_{33} \end{bmatrix}; \\
[q_b] &= \begin{bmatrix} 0 & 0 & \tilde{q}_{31} \\ 0 & 0 & \tilde{q}_{32} \\ 0 & 0 & 0 \end{bmatrix}^T; [q_s] = \begin{bmatrix} \tilde{q}_{15} & 0 & 0 \\ 0 & \tilde{q}_{24} & 0 \end{bmatrix}^T; \quad (7) \\
[m] &= \begin{bmatrix} \tilde{m}_{11} & 0 & 0 \\ 0 & \tilde{m}_{22} & 0 \\ 0 & 0 & \tilde{m}_{33} \end{bmatrix}; \\
[\eta] &= \begin{bmatrix} \tilde{\eta}_{11} & 0 & 0 \\ 0 & \tilde{\eta}_{22} & 0 \\ 0 & 0 & \tilde{\eta}_{33} \end{bmatrix}; [\alpha] = \begin{bmatrix} \tilde{\alpha}_1 \\ \tilde{\alpha}_2 \\ 0 \\ 0 \\ 0 \end{bmatrix}; \\
[p] &= \begin{bmatrix} \tilde{p}_1 \\ \tilde{p}_2 \\ \tilde{p}_3 \end{bmatrix}; [\lambda] = \begin{bmatrix} \tilde{\lambda}_1 \\ \tilde{\lambda}_2 \\ \tilde{\lambda}_3 \end{bmatrix}
\end{aligned}$$

The explicit forms of the reduced material properties can be represented as follows

$$\begin{aligned}
\tilde{C}_{11} &= C_{11} - \frac{C_{13}^2}{C_{33}}; \tilde{C}_{12} = C_{12} - \frac{C_{13}C_{23}}{C_{33}}; \tilde{C}_{22} = C_{22} - \frac{C_{23}^2}{C_{33}}; \tilde{C}_{44} = C_{44}; \tilde{C}_{55} = C_{55}; \tilde{C}_{66} = C_{66} \\
\tilde{e}_{31} &= e_{31} - \frac{C_{13}e_{33}}{C_{33}}; \tilde{e}_{32} = e_{32} - \frac{C_{23}e_{33}}{C_{33}}; \\
\tilde{e}_{15} &= e_{15}; \tilde{e}_{24} = e_{24}; \\
\tilde{q}_{31} &= q_{31} - \frac{C_{13}q_{33}}{C_{33}}; \tilde{q}_{32} = q_{32} - \frac{C_{23}q_{33}}{C_{33}}; \\
\tilde{q}_{15} &= q_{15}; \tilde{q}_{24} = q_{24}; \quad (8) \\
\tilde{\eta}_{11} &= \eta_{11}; \tilde{\eta}_{22} = \eta_{22}; \tilde{\eta}_{33} = \eta_{33} + \frac{e_{33}^2}{C_{33}}; \\
\tilde{m}_{11} &= m_{11}; \tilde{m}_{22} = m_{22}; \tilde{m}_{33} = m_{33} + \frac{e_{33}q_{33}}{C_{33}}; \\
\tilde{\alpha}_1 &= \alpha_1 - \frac{C_{13}\alpha_3}{C_{33}}; \tilde{\alpha}_2 = \alpha_2 - \frac{C_{23}\alpha_3}{C_{33}}; \\
\tilde{p}_1 &= p_1; \tilde{p}_2 = p_2; \tilde{p}_3 = p_3 + \frac{e_{33}\alpha_3}{C_{33}}; \tilde{\lambda}_1 = \lambda_1; \\
\tilde{\lambda}_2 &= \lambda_2; \tilde{\lambda}_3 = \lambda_3 + \frac{q_{33}\alpha_3}{C_{33}}.
\end{aligned}$$

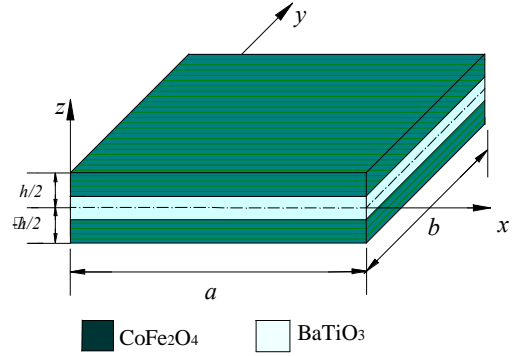


Fig. 1 MEE plate geometry

## 2.1 Problem statement

The layered METE plate subjected to thermal load is considered for evaluation. The geometry and dimensions of the plate are schematically depicted in Fig. 1. The plate has length  $a$ , width  $b$  and uniform thickness  $h$ . In the unstressed reference configuration, the METE plate occupies the region,  $[0, a] \times [0, b] \times [-\frac{h}{2}, \frac{h}{2}]$ . Also, the axes are parallel to the edges of the METE plate. Further,  $(z = 0)$  corresponds to the mid-plane.

## 2.2 METE plate kinematics

The kinematics of the METE plates is assumed to follow Reddy's third order shear deformation theory. The displacement fields satisfying the zero transverse shear stress at the top and bottom surfaces of METE plate can be represented as follows

$$\begin{aligned}
u &= u_0 + z\theta_x - \frac{4}{3h^2}z^3\left(\theta_x + \frac{\partial w_0}{\partial x}\right) \\
v &= v_0 + z\theta_y - \frac{4}{3h^2}z^3\left(\theta_y + \frac{\partial w_0}{\partial y}\right) \\
w &= w_0
\end{aligned} \quad (9)$$

$u_0$ ,  $v_0$ ,  $w_0$ ,  $\theta_x$  and  $\theta_y$  are the unknown mid-plane displacements. The relationship between the strains and the displacement components are established as follows

$$\begin{aligned}
\epsilon_x &= \frac{\partial u}{\partial x} = \frac{\partial u_0}{\partial x} + z\frac{\partial \theta_x}{\partial x} - \frac{4}{3h^2}z^3\left(\frac{\partial \theta_x}{\partial x} + \frac{\partial^2 w_0}{\partial x^2}\right) \\
\epsilon_y &= \frac{\partial v}{\partial y} = \frac{\partial v_0}{\partial y} + z\frac{\partial \theta_y}{\partial y} - \frac{4}{3h^2}z^3\left(\frac{\partial \theta_y}{\partial y} + \frac{\partial^2 w_0}{\partial y^2}\right) \\
\gamma_{xy} &= \frac{\partial u}{\partial y} + \frac{\partial v}{\partial x} = \frac{\partial u_0}{\partial y} + \frac{\partial v_0}{\partial x} + z\left(\frac{\partial \theta_x}{\partial y} + \frac{\partial \theta_y}{\partial x}\right) - \frac{4}{3h^2}z^3\left(\frac{\partial \theta_x}{\partial y} + \frac{\partial \theta_y}{\partial x} + 2\frac{\partial^2 w_0}{\partial x \partial y}\right)
\end{aligned}$$

$$\begin{aligned}\gamma_{yz} &= \theta_y + \frac{\partial w_0}{\partial y} - \frac{4}{h^2} z^2 \left( \theta_y + \frac{\partial w_0}{\partial y} \right) \\ \gamma_{xz} &= \theta_x + \frac{\partial w_0}{\partial x} - \frac{4}{h^2} z^2 \left( \theta_x + \frac{\partial w_0}{\partial x} \right)\end{aligned}\quad (10)$$

Splitting the overall strains as bending  $\{\varepsilon_b\}$  and shear  $\{\varepsilon_s\}$  strains, it can be expressed as

$$\begin{aligned}\{\varepsilon_b\} &= \{\varepsilon_x \ \varepsilon_y \ \gamma_{xy}\}^T, \{\varepsilon_s\} = \{\gamma_{xz} \ \gamma_{yz}\}^T \\ \{\varepsilon_b\} &= \begin{Bmatrix} \varepsilon_x \\ \varepsilon_y \\ \gamma_{xy} \end{Bmatrix} = \begin{bmatrix} \frac{\partial}{\partial x} & 0 & 0 \\ 0 & \frac{\partial}{\partial y} & 0 \\ \frac{\partial}{\partial y} & \frac{\partial}{\partial x} & 0 \end{bmatrix} \begin{Bmatrix} u_0 \\ v_0 \\ w_0 \end{Bmatrix} + \\ &\quad (z + c_1 z^3) \begin{bmatrix} \frac{\partial}{\partial x} & 0 \\ 0 & \frac{\partial}{\partial y} \end{bmatrix} \begin{Bmatrix} \theta_x \\ \theta_y \end{Bmatrix} + c_1 z^3 \begin{bmatrix} \frac{\partial}{\partial x} & 0 \\ 0 & \frac{\partial}{\partial y} \end{bmatrix} \begin{Bmatrix} \kappa_x \\ \kappa_y \end{Bmatrix} \\ \{\varepsilon_s\} &= \begin{Bmatrix} \gamma_{xz} \\ \gamma_{yz} \end{Bmatrix} = \begin{bmatrix} 0 & 0 & \frac{\partial}{\partial x} \\ 0 & 0 & \frac{\partial}{\partial y} \end{bmatrix} \begin{Bmatrix} u_0 \\ v_0 \\ w_0 \end{Bmatrix} + \begin{bmatrix} 1 & 0 \\ 0 & 1 \end{bmatrix} \begin{Bmatrix} \theta_x \\ \theta_y \end{Bmatrix} + \\ &\quad c_2 z^2 \begin{bmatrix} 1 & 0 \\ 0 & 1 \end{bmatrix} \begin{Bmatrix} \theta_x \\ \theta_y \end{Bmatrix} + \begin{bmatrix} 1 & 0 \\ 0 & 1 \end{bmatrix} \begin{Bmatrix} \kappa_x \\ \kappa_y \end{Bmatrix}\end{aligned}\quad (11)$$

where

$$\begin{aligned}\kappa_x &= \frac{\partial w_0}{\partial x}, \kappa_y = \frac{\partial w_0}{\partial y}, c_1 = -\frac{4}{3h^2}, \\ c_2 &= -\frac{4}{h^2}\end{aligned}\quad (12)$$

### 2.3 Finite element formulation

The FE model of the METE plate is developed through eight noded isoparametric quadrilateral element. The converged mesh size of (10×10) is employed for the analysis. The shape functions corresponding to the eight noded isoparametric element in the natural coordinate  $(\xi, \eta)$  system can be represented as follows

$$\begin{aligned}N_1(\xi, \eta) &= -\frac{1}{4}(1-\xi)(1-\eta)(1+\xi+\eta); \\ N_2(\xi, \eta) &= \frac{1}{2}(1-\xi)(1+\xi)(1-\eta); \\ N_3(\xi, \eta) &= -\frac{1}{4}(1+\xi)(1-\eta)(1-\xi+\eta); \\ N_4(\xi, \eta) &= \frac{1}{2}(1+\xi)(1+\eta)(1-\eta); \\ N_5(\xi, \eta) &= -\frac{1}{4}(1+\xi)(1+\eta)(1-\xi-\eta); \\ N_6(\xi, \eta) &= \frac{1}{2}(1-\xi)(1+\xi)(1+\eta); \\ N_7(\xi, \eta) &= -\frac{1}{4}(1-\xi)(1+\eta)(1+\xi-\eta); \\ N_8(\xi, \eta) &= \frac{1}{2}(1-\xi)(1+\eta)(1-\eta)\end{aligned}\quad (13)$$

Further, the degrees of freedom corresponding to displacement (translational-  $\{d_t\}$ , rotational-  $\{d_r\}$  and higher-order rotational  $\{d_{r*}\}$ ), magnetic ( $\psi$ ) and electric potentials ( $\phi$ ) are represented through shape functions as follows

$$\begin{aligned}\{d_t\} &= [N_t(\xi, \eta)] \{d_t^e\}, \{d_r\} = [N_r(\xi, \eta)] \{d_r^e\}, \\ \{d_{r*}\} &= [N_{r*}(\xi, \eta)] \{d_{r*}^e\}, \\ \phi &= [N_\phi(\xi, \eta)] \{\phi^e\}, \psi = [N_\psi(\xi, \eta)] \{\psi^e\}\end{aligned}\quad (14)$$

where

$$\begin{aligned}[N_t(\xi, \eta)] &= \begin{bmatrix} N_1 & 0 & 0 & N_8 & 0 & 0 \\ 0 & N_1 & 0 & \dots & 0 & N_8 \\ 0 & 0 & N_1 & 0 & 0 & N_8 \end{bmatrix}; \\ [N_r(\xi, \eta)] &= [N_{r*}(\xi, \eta)] = \begin{bmatrix} N_1 & 0 & N_8 & 0 \\ 0 & N_1 & 0 & N_8 \end{bmatrix}; \\ [N_\phi(\xi, \eta)] &= [N_\psi(\xi, \eta)] = [N_1 \ N_2 \ N_3 \ \dots \ N_8] \\ \{d_t^e\} &= [\{d_{t1}^e\}^T \ \{d_{t2}^e\}^T \ \dots \ \{d_{t8}^e\}^T]^T, \\ \{d_r^e\} &= [\{d_{r1}^e\}^T \ \{d_{r2}^e\}^T \ \dots \ \{d_{r8}^e\}^T]^T, \\ \{d_{r*}^e\} &= [\{d_{r*1}^e\}^T \ \{d_{r*2}^e\}^T \ \dots \ \{d_{r*8}^e\}^T]^T \\ \{d_{ti}\} &= [u_{0i} \ v_{0i} \ w_{0i}]^T, \\ \{d_{ri}\} &= [\theta_{xi} \ \theta_{yi}]^T, \{d_{r*i}\} = [\kappa_{xi} \ \kappa_{yi}]^T \\ &\quad (i = 1, 2, 3 \dots 8)\end{aligned}\quad (15)$$

In order to calculate the strain, stress and other static parameters, it is required to establish the partial derivatives of shape functions with respect to the Cartesian coordinates ( $x$  and  $y$ ). Also, since the shape functions are not directly functions of  $x$  and  $y$  but of the natural coordinates  $(\xi, \eta)$ , the determination of Cartesian partial derivatives is not trivial. To this end, transformation to connect the natural and Cartesian coordinates and further establish the strain-displacement matrices in Cartesian coordinate are carried out through Jacobian matrix as illustrated in Appendix-A.

Meanwhile, the strains presented in the Eq. (11) can be expressed in terms of FE parameters as follows

$$\begin{aligned}\{\varepsilon_b\} &= [B_{tb}] \{d_t^e\} + z [B_{rb}] \{d_r^e\} + \\ &\quad c_1 z^3 [B_{rb}] \{d_r^e\} + c_1 z^3 [B_{rb}] \{d_{r*}^e\} \\ \{\varepsilon_s\} &= [B_{ts}] \{d_t^e\} + [B_{rs}] \{d_r^e\} + \\ &\quad c_2 z^2 [B_{rs}] \{d_r^e\} + c_2 z^2 [B_{rs}] \{d_{r*}^e\}\end{aligned}\quad (16)$$

The electric and magnetic field can be established as follows (Moita *et al.* 2009)

$$E = [B_\phi] \{\phi^e\}; \quad H = [B_\psi] \{\psi^e\}\quad (17)$$

The nodal shape function derivative matrices  $[B_{tb}]$ ,  $[B_{rb}]$ ,  $[B_{ts}]$  and  $[B_{rs}]$  are illustrated as follows

$$\begin{aligned}[B_{tb}] &= [B_{tb1} \ B_{tb2} \ \dots \ B_{tb8}], \\ [B_{rb}] &= [B_{rb1} \ B_{rb2} \ \dots \ B_{rb8}], \\ [B_{ts}] &= [B_{ts1} \ B_{ts2} \ \dots \ B_{ts8}], \\ [B_{rs}] &= [B_{rs1} \ B_{rs2} \ \dots \ B_{rs8}], \\ [B_\phi] &= [B_{\phi1} \ B_{\phi2} \ \dots \ B_{\phi8}], \\ [B_\psi] &= [B_{\psi1} \ B_{\psi2} \ \dots \ B_{\psi8}]\end{aligned}\quad (18)$$

The strain-displacement sub matrices appearing in Eq. (18) can be explicitly illustrated as follows

$$\begin{aligned}
[B_{tbi}] &= \begin{bmatrix} \frac{\partial N_i}{\partial x} & 0 & 0 \\ 0 & \frac{\partial N_i}{\partial y} & 0 \\ \frac{\partial N_i}{\partial y} & \frac{\partial N_i}{\partial x} & 0 \end{bmatrix}; [B_{rb}] = \begin{bmatrix} \frac{\partial N_i}{\partial x} & 0 \\ 0 & \frac{\partial N_i}{\partial y} \\ \frac{\partial N_i}{\partial y} & \frac{\partial N_i}{\partial x} \end{bmatrix}; \\
[B_{ts}] &= \begin{bmatrix} 0 & 0 & \frac{\partial N_i}{\partial x} \\ 0 & 0 & \frac{\partial N_i}{\partial y} \end{bmatrix}; [B_{rs}] = \begin{bmatrix} N_i & 0 \\ 0 & N_i \end{bmatrix}; \\
[B_\phi] &= [B_\psi] = \begin{bmatrix} 0 \\ 0 \\ -N_i/h \end{bmatrix}
\end{aligned} \quad (19)$$

## 2.4 Equations of motion

Hamilton's principle is invoked to derive the equations of motion of the METE plates as follows (Vinyas and Kattimani 2017d)

$$\delta T_p = \frac{1}{2} \sum_{n=1}^N \int_{\Omega^n} \delta \left( \{\varepsilon_b\}^T \{\sigma_b\} \right) d\Omega^n + \frac{1}{2} \sum_{n=1}^N \int_{\Omega^k} \delta \left( \{\varepsilon_b\}^T \{\sigma_b\} \right) d\Omega^n$$

$$\begin{aligned}
& - \frac{1}{2} \sum_{n=1}^N \int_{\Omega^n} \delta \left( \{E\}^T \{D\} \right) d\Omega^n \\
& - \frac{1}{2} \sum_{n=1}^N \int_{\Omega^n} \delta \left( \{H\}^T \{B\} \right) d\Omega^n - \int_A \delta \left( \{d_t\}^T \{f\} \right) dA \\
& - \int_A \delta \left( \{\phi\}^T \{Q^\phi\} \right) dA - \int_A \delta \left( \{\psi\}^T \{Q^\psi\} \right) dA
\end{aligned} \quad (20)$$

$$\delta T_k = \int_{\Omega^n} \delta \left( \{d_t\}^T \rho \{\ddot{d}_t\} \right) d\Omega^n \quad (21)$$

$$\delta T_p + \delta T_k = 0 \quad (22)$$

where,  $N$  denotes the total number of layers in the METE plates.  $\{f\}$ ,  $Q^\phi$  and  $Q^\psi$  are the mechanical field force, electric surface charge density and magnetic flux density, respectively acting over an area  $A$ . The volume of the  $n^{th}$  layer is represented by  $\Omega^n$ . The contribution of rotary inertia is very minimal. Hence, for the computational ease it may be neglected. Substituting Eqs. (1)-(3) and (16)-(19), Eq. (22) can be represented as follows

$$\begin{aligned}
& \frac{1}{2} \sum_{n=1}^N \int_{\Omega^n} \delta \left( \{d_{r*}\}^T [B_{rb}]^T c_1 z^3 + \{d_r\}^T [B_{rb}]^T c_1 z^3 \right. \\
& \quad \left. + \{d_r\}^T [B_{rb}]^T z + \{d_t\}^T [B_{tb}]^T \right) * \\
& \quad \left\{ \left( [C_b][B_{tb}]\{d_t\} + z[C_b][B_{rb}]\{d_r\} + c_1 z^3 \right. \right. \\
& \quad \left. \left. - \{e\}[E] - \{q\}[H] - \{\alpha\}\Delta T \right. \right. \\
& \quad \left. \left. + [C_b][B_{rb}]\{d_r\} + c_1 z^3 [C_b][B_{rb}]\{d_{r*}\} \right) \right\} \Omega^n \\
& + \frac{1}{2} \sum_{n=1}^N \int_{\Omega^n} \delta \left( \{d_{r*}\}^T [B_{rs}]^T c_2 z^2 + \{d_r\}^T [B_{rs}]^T c_2 z^2 \right. \\
& \quad \left. + \{d_r\}^T [B_{rs}]^T + \{d_t\}^T [B_{ts}]^T \right) * \\
& \quad \left\{ \left( [C_s][B_{ts}]\{d_t\} + z[C_s][B_{rs}]\{d_r\} \right. \right. \\
& \quad \left. \left. - [e][E] - [q][H] \right) \right\} \Omega^n
\end{aligned} \quad (23)$$

$$\begin{aligned}
& + c_2 z^2 [C_s][B_{rs}]\{d_r\} + c_2 z^2 [C_s][B_{rs}]\{d_{r*}\} \Big\} \Omega^n \\
& - \frac{1}{2} \sum_{n=1}^N \delta \int_{\Omega^n} \{ \phi \}^T [B_\phi]^T ([e_b]^T [B_{ib}]\{d_i\} + [e_b]^T \\
& \quad z[B_{rb}]\{d_r\} + [e_b]^T c_1 z^3 [B_{rb}]\{d_r\} + [e_b]^T c_1 z^3 [B_{rb}]\{d_{r*}\} \\
& \quad + [e_s]^T [B_{ts}]\{d_t\} + [e_s]^T [B_{rs}]\{d_r\} + [e_s]^T \\
& \quad c_2 z^2 [B_{rs}]\{d_r\} + [e_s]^T c_2 z^2 [B_{rs}]\{d_{r*}\} + [e_s]^T c_2 z^2 \\
& \quad [B_{rs}]\{d_{r*}\} + [\eta][B_\phi]\{\phi\} + [m][B_\psi]\{\psi\} + [p]\Delta T) \Big\} \Omega^n \\
& - \frac{1}{2} \sum_{n=1}^N \delta \int_{\Omega^n} \{ \psi \}^T [B_\psi]^T ([q_b]^T z[B_{rb}]\{d_r\} + [q_b]^T \\
& \quad z[B_{rb}]\{d_r\} + [q_b]^T c_1 z^3 [B_{rb}]\{d_r\} + [q_b]^T c_1 z^3 [B_{rb}]\{d_{r*}\} \\
& \quad + [q_s]^T [B_{ts}]\{d_t\} + [q_s]^T [B_{rs}]\{d_r\} + [q_s]^T \\
& \quad c_2 z^2 [B_{rs}]\{d_r\} + [q_s]^T c_2 z^2 [B_{rs}]\{d_{r*}\} \\
& \quad + [m][B_\phi]\{\phi\} + [\psi][\mu][B_\psi] + [\lambda]\Delta T) \Big\} \Omega^n \\
& - \int_A \delta \left( \{ \phi \}^T \{ F_\phi^e \} \right) - \int_A \delta \left( \{ \psi \}^T \{ F_\psi^e \} \right) + [M_{ii}^e] \{ \ddot{d}_i^e \} = 0
\end{aligned}$$

Further, splitting the terms based on the coefficients of  $\{d_t^e\}^T$ ,  $\{d_r^e\}^T$ ,  $\{d_{r*}^e\}^T$ ,  $\{\phi^e\}^T$  and  $\{\psi^e\}^T$ , we obtain the equations of motion as follows

$$\begin{aligned}
& [M_{ii}^e] \{ \ddot{d}_i^e \} + [K_{ii}^e] \{ d_i^e \} + [K_{ir}^e] \{ d_r^e \} + [K_{ir*}^e] \{ d_{r*}^e \} \\
& + [K_{i\phi}^e] \{ \phi^e \} + [K_{i\psi}^e] \{ \psi^e \} = [F_{\Delta Trb1}^e] \\
& [K_{rr}^e] \{ d_r^e \} + [K_{rr*}^e] \{ d_{r*}^e \} + [K_{r\phi}^e] \{ \phi^e \} + [K_{r\psi}^e] \{ \psi^e \} = [F_{\Delta Trb24}^e] \\
& [K_{r*}^e] \{ d_t^e \} + [K_{r*}^e] \{ d_r^e \} + [K_{r*}^e] \{ d_{r*}^e \} \\
& + [K_{r*}^e] \{ \phi^e \} + [K_{r*}^e] \{ \psi^e \} = [F_{\Delta Trb4}^e] \\
& [K_{t\phi}^e] \{ d_t^e \} + [K_{t\phi}^e] \{ d_r^e \} + [K_{t\phi}^e] \{ d_{r*}^e \} \\
& - [K_{\phi\phi}^e] \{ \phi^e \} - [K_{\phi\psi}^e] \{ \psi^e \} = \{ F_\phi^e \} + \{ F_{\phi-\Delta T}^e \} \\
& [K_{t\psi}^e] \{ d_t^e \} + [K_{t\psi}^e] \{ d_r^e \} + [K_{t\psi}^e] \{ d_{r*}^e \} \\
& - [K_{\psi\psi}^e] \{ \psi^e \} - [K_{\psi\phi}^e] \{ \phi^e \} = \{ F_\psi^e \} + \{ F_{\psi-\Delta T}^e \}
\end{aligned} \quad (24)$$

in which,  $\{F_{\Delta Trb1}^e\}$ ,  $\{F_{\Delta Trb24}^e\}$  and  $\{F_{\Delta Trb4}^e\}$  are the thermal load vectors. In addition pyroelectric load vector, pyromagnetic load vector, electric load vector and magnetic load vector can be represented as  $\{F_{\phi-\Delta T}^e\}$ ,  $\{F_{\psi-\Delta T}^e\}$ ,  $\{F_\phi^e\}^T$ ,  $\{F_\psi^e\}^T$ , respectively. The different stiffness matrices and force matrices appearing in Eq. (24) and the associated rigidity matrices are explicitly represented in Appendix-B.

## 3. Results and discussion

In this section, several numerical examples are presented to evaluate the static response of METE plates subjected to the thermal environment using the FE formulation derived earlier. To this end, the METE with dimensions  $a=b=1$  m;  $h=0.3$  m are considered for

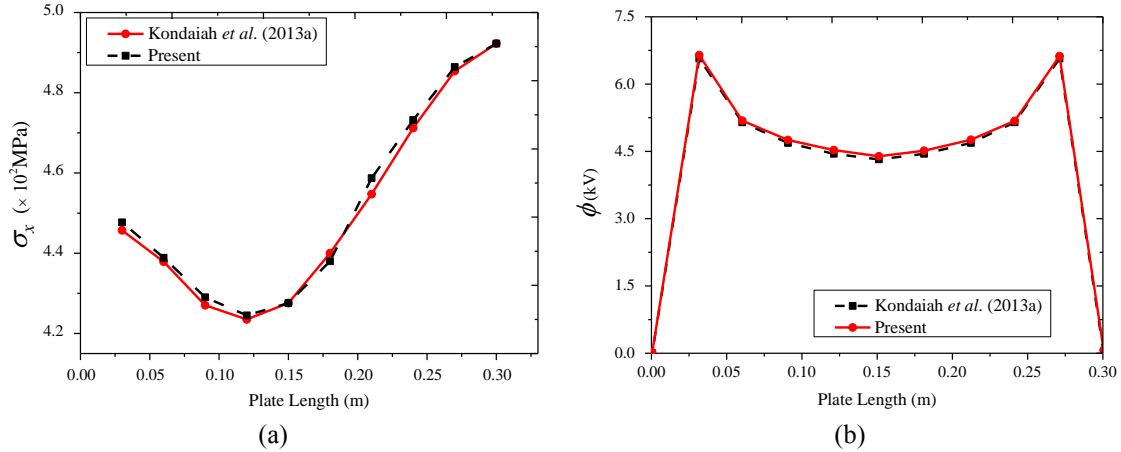


Fig. 2 Validation plots of (a) normal stress  $\sigma_x$  (b) electric potential  $\phi$  of METE plate subjected to uniform temperature gradient ( $a=b=0.3$  m;  $h=0.006$  m)

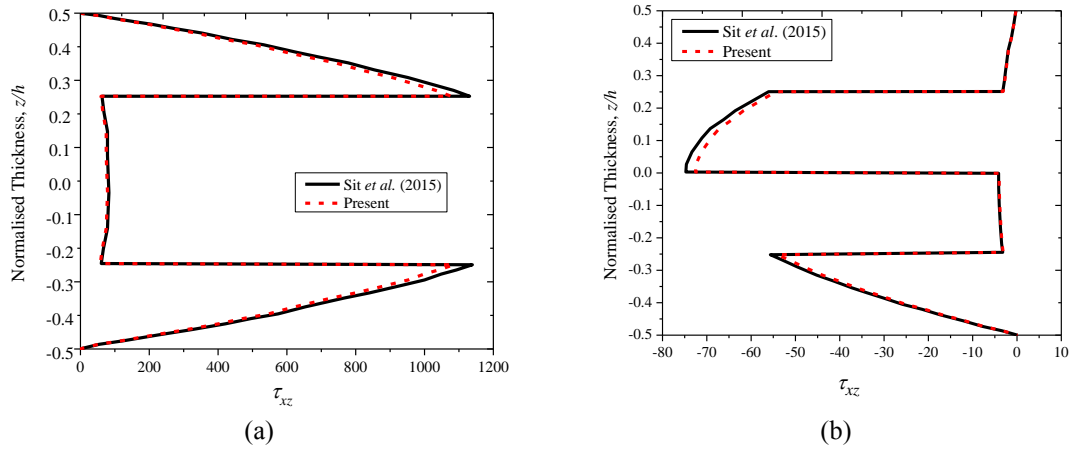


Fig. 3 Validation plots for shear stress  $\tau_{xz}$  of (a) symmetric cross-ply (b) anti-symmetric cross-ply composite plate subjected to thermal loading ( $a/h=5$ )

evaluation. The mechanical boundary constraints adopted in this study can be represented as follows

Clamped edge (C):

$$u = v = w = \theta_x = \theta_y = \kappa_x = \kappa_y = 0$$

Simply supported edge (S):

$$u = \theta_x = \kappa_x \neq 0; v = w = 0 \quad \text{at } x^I = 0, a \quad (25)$$

$$v = \theta_y = \kappa_y \neq 0; u = w = 0 \quad \text{at } y^I = 0, b$$

Similarly, the closed-circuit and open-circuit electro-magnetic boundary conditions adopted are as follows (Shooshtari and Razavi 2016)

Closed-circuit:

$$\phi = \psi = 0 \quad (z = \pm \frac{h}{2})$$

Open-circuit:

$$D_z = B_z = 0 \quad (z = \pm \frac{h}{2}) \quad (26)$$

Numerical examples are discussed in detail to evaluate the influence of different magnitude of thermal loads, electro-magnetic boundary conditions, stacking sequences, aspect ratio and pyrocoupling effects.

### 3.1 Verification of results

In this section, the credibility of the present FE model to assess the coupled static response of METE plates has been verified. A converged mesh size of  $10 \times 10$  has been used for the analysis. The problem of METE plates subjected to uniform temperature load of 100 K, as illustrated in Kondaiah *et al.* (2013a) is considered and solved using the present method. Fig. 2(a) and (b) draw the conclusion that the proposed higher order FE model yields similar results as that of Kondaiah *et al.* (2013a). Therefore, it can be justified that the proposed FE formulation accurately incorporates the coupling fields.

Further, the validation study has been extended to justify the credibility of the proposed FE formulation to incorporate higher order terms and predict the thermal response of thick plates accurately. To the best of authors' knowledge there are no articles reported on the static behaviour METE thick plate in thermal environment. Hence, the validation of the present FE formulation is carried out by considering a numerical example of composite plates subjected to thermal loading as illustrated in Sit *et al.* (2015). The geometric and material properties are retained similar to that of Sit *et al.* (2015). From Figs.

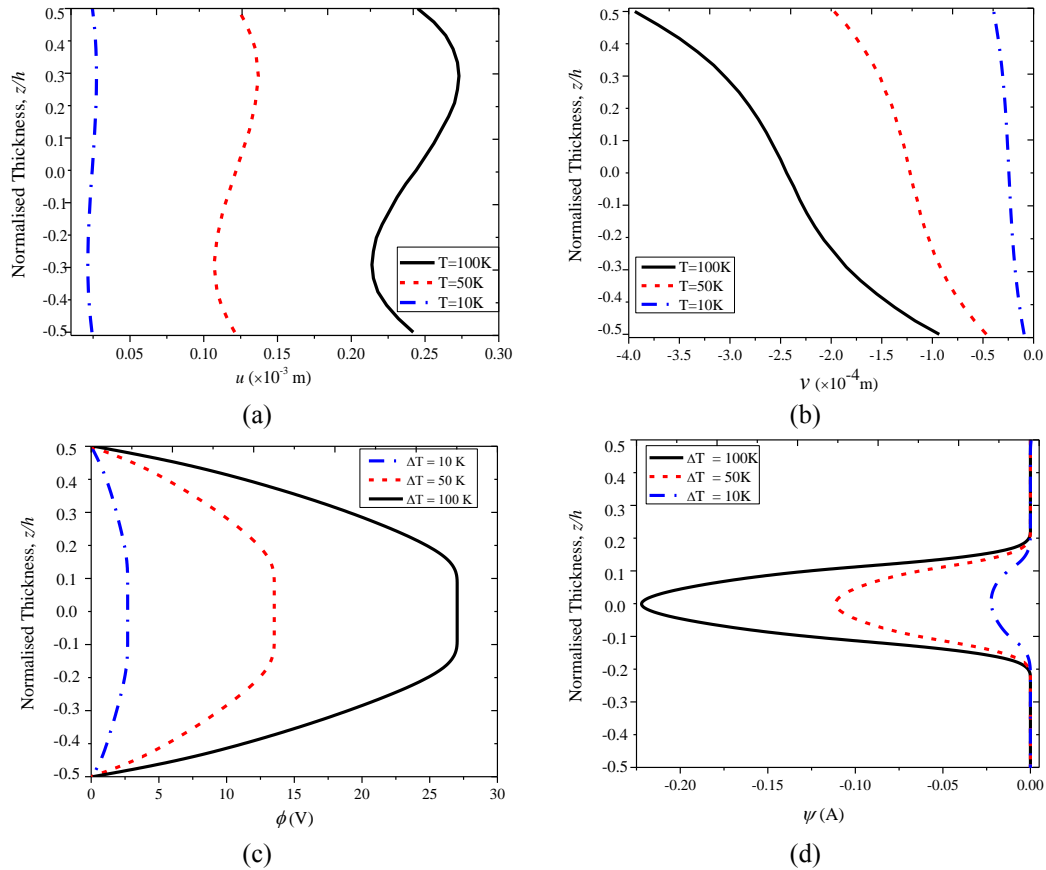


Fig. 4 Effect of different magnitude of temperature gradient on (a) displacement component  $u$  (b) displacement component  $v$  (c) electric potential,  $\phi$  (d) magnetic potential,  $\psi$  (BFB, SSSS and closed-circuit condition)

Table 1 Material properties corresponding to different volume fraction  $V_f$  of  $\text{BaTiO}_3 - \text{CoFe}_2\text{O}_4$  (Kondaiah *et al.*, Vinyas and Kattimani 2017)

Material property	Material constants	Piezomagnetic Material (F)	Piezoelectric material (B)
Elastic constants (GPa)	$C_{11}=C_{22}$	286	166
	$C_{12}$	173	77
	$C_{13}=C_{23}$	170	78
	$C_{33}$	269.5	162
	$C_{44}=C_{55}$	45.3	43
	$C_{66}$	56.5	44.5
Piezoelectric constants (C/m <sup>2</sup> )	$e_{31}$	0	-4.4
	$e_{33}$	0	18.6
	$e_{15}$	0	11.6
Dielectric constant ( $10^{-9}$ C <sup>2</sup> /Nm <sup>2</sup> )	$\epsilon_{11}=\epsilon_{22}$	0.08	11.2
	$\epsilon_{33}$	0.093	12.6
Magnetic permeability ( $10^{-4}$ Ns <sup>2</sup> /C <sup>2</sup> )	$\mu_{11}=\mu_{22}$	5.9	0.05
	$\mu_{33}$	1.57	0.1
Piezomagnetic constants(N/Am)	$q_{31}$	580	0
	$q_{33}$	700	0
	$q_{15}$	560	0
Magneto-electric constant ( $10^{-12}$ Ns/VC)	$m_{11}=m_{22}$	0	0
	$m_{33}$	0	0
Pyroelectric constant ( $10^{-7}$ C/m <sup>2</sup> K)	$p_3$	0	0
Pyromagnetic constant ( $10^{-5}$ C/m <sup>2</sup> K)	$\lambda_3$	0	0
Thermal expansion coefficient ( $10^{-6}$ K <sup>-1</sup> )	$\alpha_1=\alpha_2$	10	15.7
	$\alpha_3$	10	6.4
Density (kg/m <sup>3</sup> )	$\rho$	5300	5800

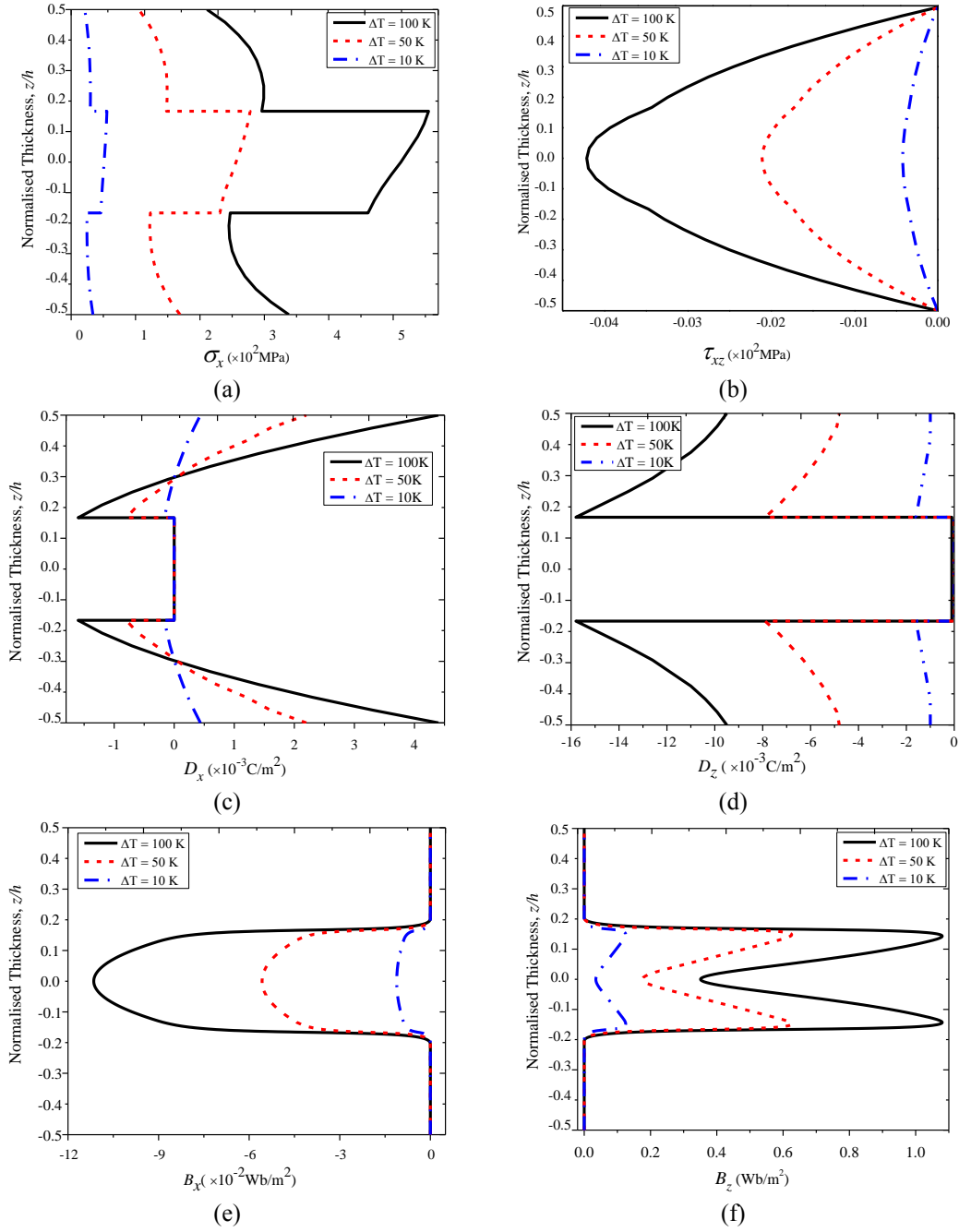


Fig. 5 Effect of different magnitude of temperature gradient on (a)  $\sigma_x$  (b)  $\tau_{xz}$  (c)  $D_x$  (d)  $D_z$  (e)  $B_x$  (f)  $B_z$  (BFB, SSSS and closed-circuit condition)

3(a) and (b) it can be inferred that the results from the present FE formulation correlates with that of Sit *et al.* (2015). Therefore, it can be concluded from these two validation studies that the proposed FE formulation effectively incorporates the coupling fields as well as higher-order terms to accurately predict the static response of METE plates.

### 3.2 Effect of temperature load

The variation of the static parameters of METE plates subjected to different magnitudes of temperature loading has been investigated. To this end, BFB stacking sequence

and closed-circuit electro-magnetic boundary condition is employed. The piezoelectric phase/layer is represented by 'B' whereas the piezomagnetic phase is denoted by 'F'. Further, three different magnitudes of temperature gradient ( $\Delta T$ ) viz. 10 K, 50 K and 100 K has been considered for the evaluation. From Figs. 4(a) and (b), it can be witnessed that as the magnitude of temperature gradient increases, the displacement component ( $u$  and  $v$ ) also significantly increases. The electric and magnetic potentials of METE plate are illustrated in Figs. 4(c) and (d), respectively. The TSĐT gives an accurate estimate of the electric and magnetic potentials in contrast to other plate theories. A parabolic variation of electric potential is noticed at the 'B'



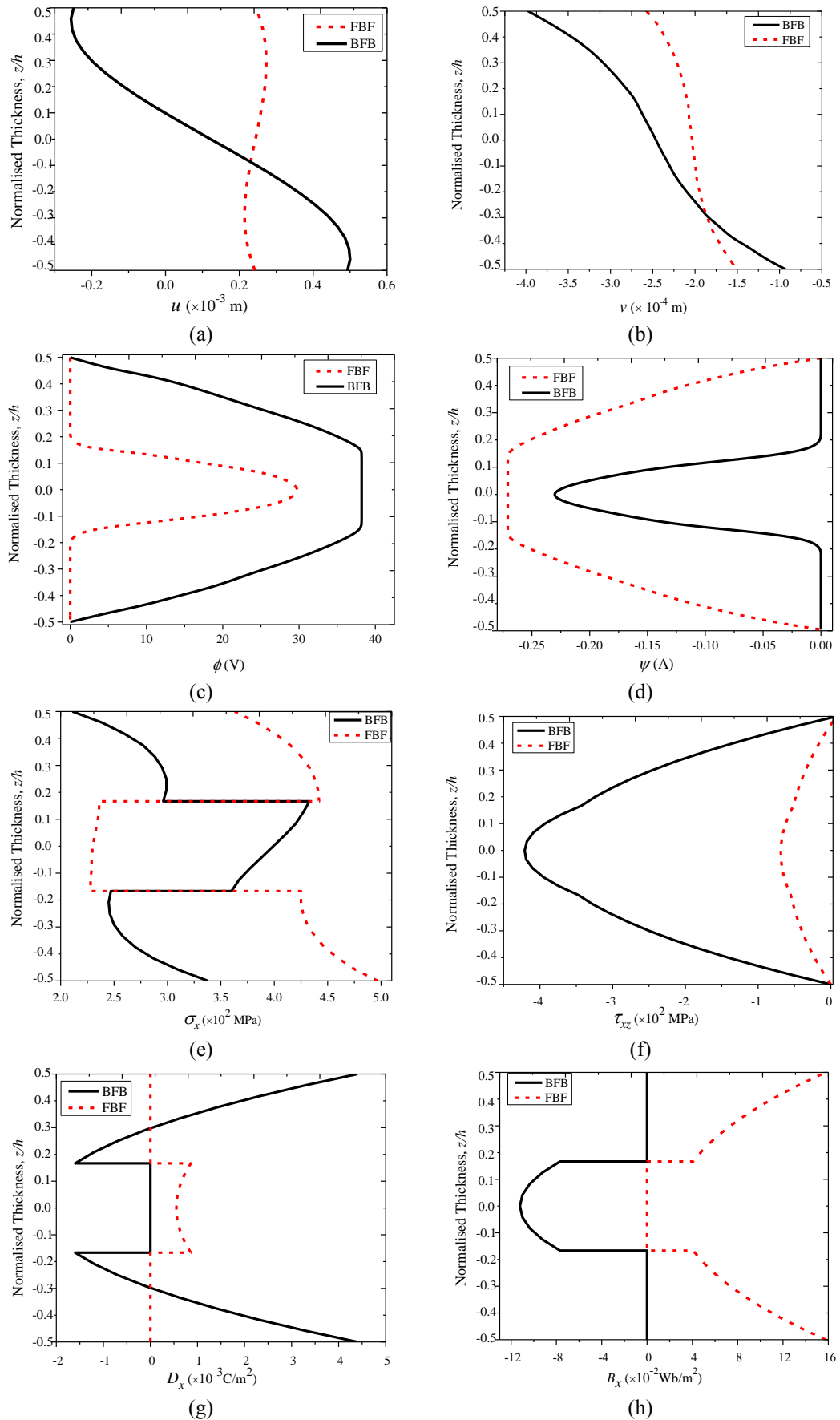


Fig. 6 Effect of stacking sequence on (a) displacement component  $u$  (b) displacement component  $v$  (c) electric potential  $\phi$  (d) magnetic potential  $\psi$  (e)  $\sigma_x$  (f)  $\tau_{xz}$  (g)  $D_x$  (h)  $B_x$  (i)  $D_z$  (j)  $B_z$  ( $a=b=1$  m;  $h=0.3$  m; (a)-(h): SSSS; (i) and (j)-CCCC; closed-circuit)

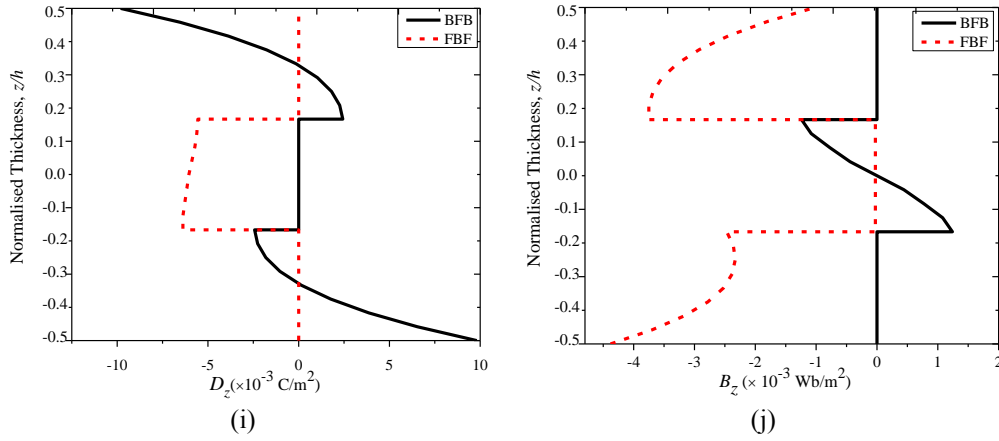


Fig. 6 Continued

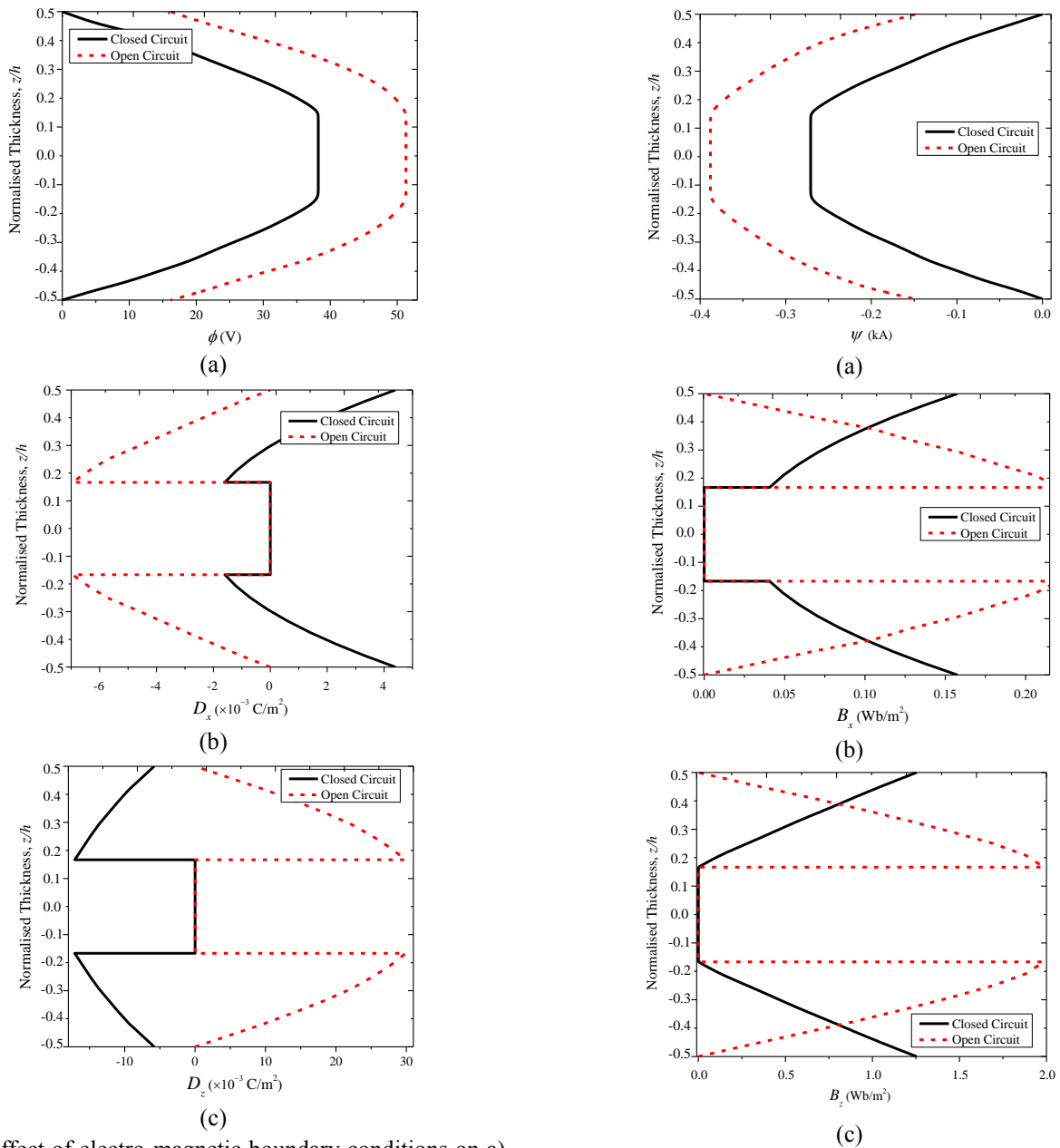


Fig. 7 Effect of electro-magnetic boundary conditions on a) electric potential  $\phi$  (b)  $D_x$  (c)  $D_z$  ( $a=b=1$  m;  $h=0.3$  m; BFB stacking sequence)

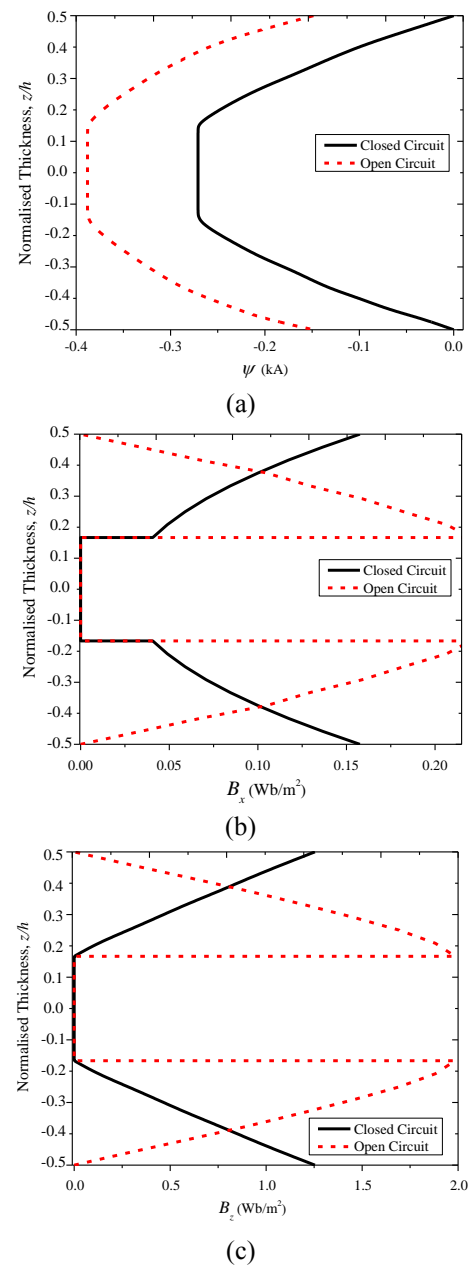


Fig. 8 Effect of electro-magnetic boundary conditions on (a) magnetic potential  $\psi$  (b)  $B_x$  (c)  $B_z$  ( $a=b=1$  m;  $h=0.3$  m; FBF stacking sequence)

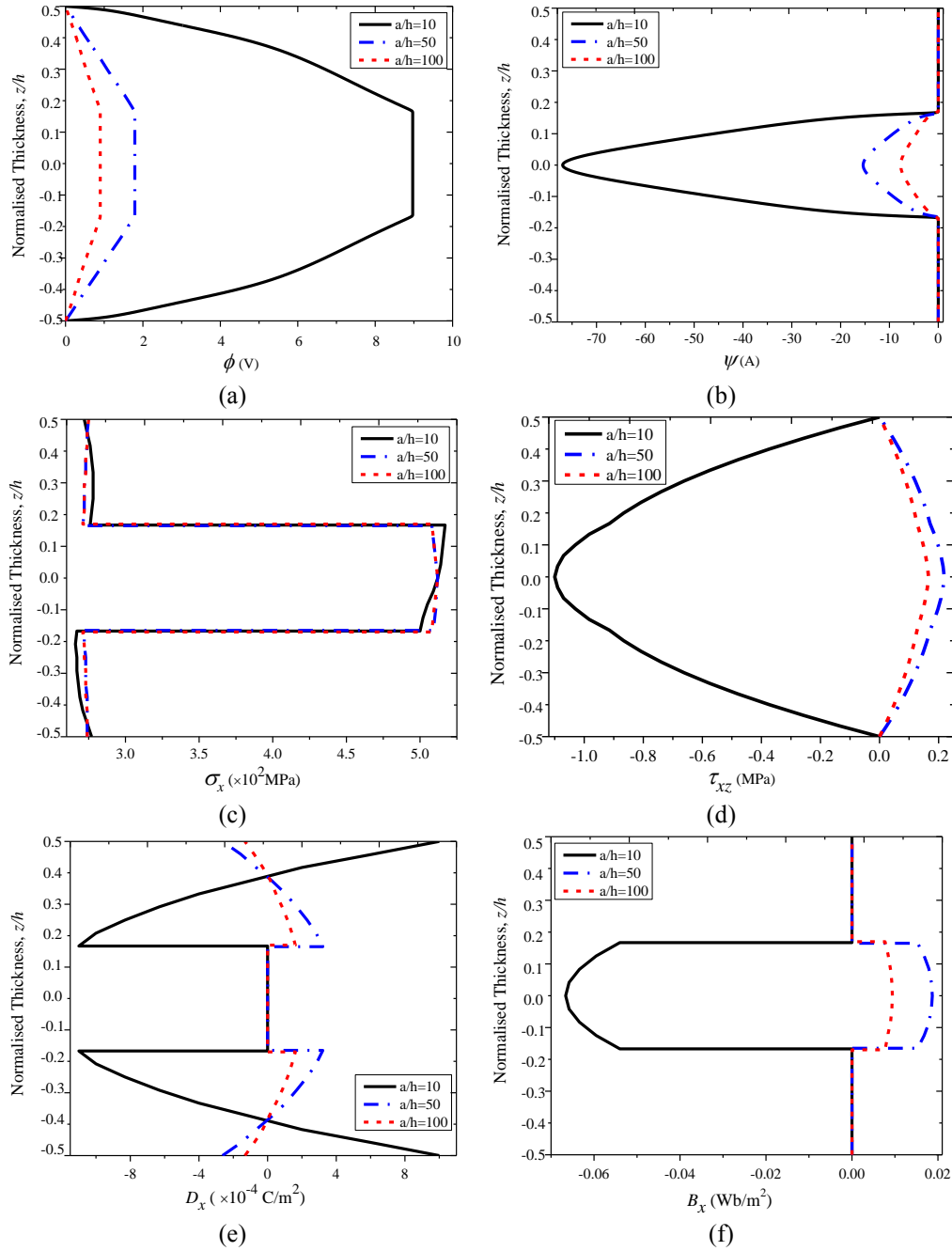


Fig. 9 Effect of  $a/h$  ratio on (a) electric potential  $\phi$  (b) magnetic potential  $\psi$  (c)  $\sigma_x$  (d)  $\tau_{xz}$  (e)  $D_x$  (f)  $B_x$  ( $a=b=1$  m;  $h=0.3$  m; CCCC; closed-circuit)

layers while it is constant at the middle ‘F’ layer. Analogously, the magnetic potential is observed only at the middle ‘F’ layer.

Meanwhile, the variations of derived components i.e., the stress components such as  $\sigma_x$  and  $\tau_{xz}$  are depicted in Figs. 5(a) and 5(b), respectively. It can be witnessed from Fig. 5(a) that the middle ‘F’ layer experiences a higher stress in comparison with the top and bottom ‘B’ layer. This may be attributed to the fact that the piezomagnetic (F) layer has the higher elastic stiffness coefficient and lower coefficient of thermal expansion compared to the piezoelectric (B) layer. Hence, the stress increases according to Eq. (1). The distribution of the shear stress

across the plate thickness is shown in Fig. 5(b). According to this figure, it is noticed that  $\tau_{xz}$  satisfy the zero shear stress condition at the top and bottom surfaces, respectively. The magnitude of all the stresses increases with a higher temperature gradient.

### 3.3 Effect of stacking sequence

The coupling stiffness of the METE plates is significantly affected by its stacking sequence (Vinyas and Kattimani 2017c). This in turn directly influences the multiphysics structural response of the overall METE plates in the thermal environment. The numerical results reveal

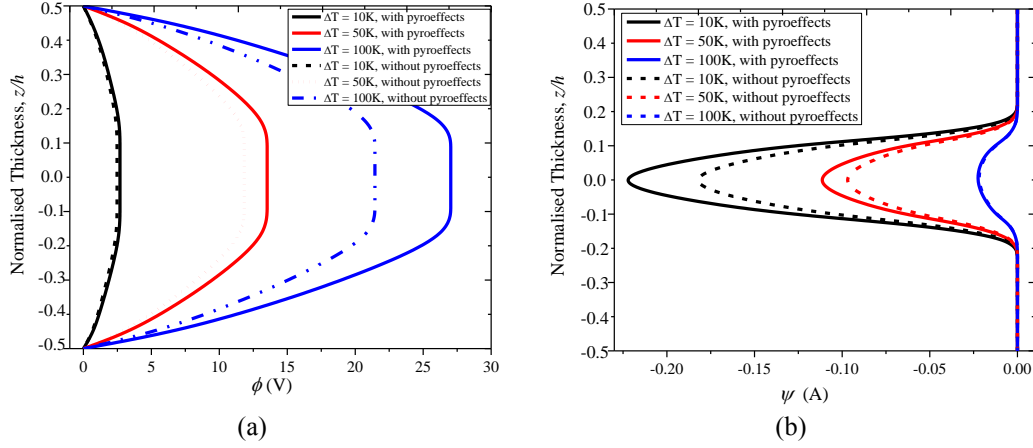


Fig. 10 Effect of pyrocoupling on (a) electric potential  $\phi$  (b) magnetic potential  $\psi$  of METE plate with different temperature gradient ( $a=b=1$  m;  $h=0.3$  m; BFB; SSSS; closed-circuit)

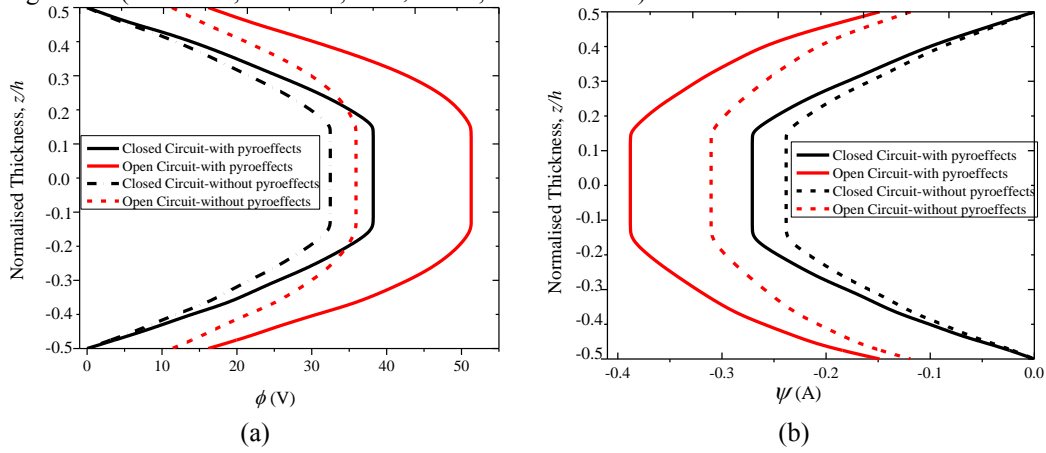


Fig. 11 Effect of pyrocoupling on (a) electric potential  $\phi$  (b) magnetic potential  $\psi$  of METE plate with different electro-magnetic boundary conditions ( $a=b=1$  m;  $h=0.3$  m; SSSS;  $\Delta T=100$  K)

Table 2 Effect of electro-magnetic boundary conditions associated with stacking sequence on the maximum value of static parameters (SSSS;  $a=b=1$  m;  $h=0.3$  m)

Static Parameter (Max. value)	BFB		FBF	
	Open circuit	Closed Circuit	Open circuit	Closed Circuit
$\phi$ (V)	51.29	38.21	45.56	31.25
$\psi$ (A)	0.29	0.23	0.39	0.27
$\sigma_x (\times 10^2 \text{ MPa})$	6.45	5.55	5.72	4.97
$\tau_{xz} (\times 10^2 \text{ MPa})$	5.88	4.21	0.94	0.69
$D_x (\times 10^{-3} \text{ C/m}^2)$	6.95	4.4	1.06	0.858
$D_z (\times 10^{-3} \text{ C/m}^2)$	29.92	17.1	17.67	11.2
$B_x (\text{Wb/m}^2)$	0.11	0.087	0.22	0.157
$B_z (\text{Wb/m}^2)$	1.14	0.91	1.98	1.25

that the displacement components  $u$  and  $v$  are higher for BFB stacking sequences, in contrast to the FBF-METE plate (Figs. 6(a) and 6(b)). It is attributed to the fact that, BFB-METE plates comprise of more number of 'B' layers, which have lesser elastic stiffness co-efficient. Hence, the overall stiffness of BFB-METE plates is lesser than the FBF-METE plates. Analogously, the comparison plots of the electric and magnetic potentials are depicted in Figs. 6(c) and 6(d), respectively. As a result of higher degree of electro-elastic coupling exhibited by two 'B' layers of BFB-

METE plate, the electric displacements are higher than FBF-METE plates. On the other hand the magnetic potential is higher for the FBF-METE plates due to higher magneto-elastic coupling.

The normal stress ( $\sigma_x$ ) and shear stress ( $\tau_{xz}$ ) for BFB and FBF METE plates under thermal loads are shown in Figs. 6(e) and 6(f), respectively. The results in these figures suggest that FBF stacking sequence yields a higher normal stress than BFB stacking sequence. This can be attributed to the fact that the higher stiffness coefficients ( $C_{11}$ ,  $C_{12}$ ,  $C_{22}$ ) of 'F' phase result in a greater coupled stressed value, according to Eq. (1). Meanwhile, this trend is reversed in case of shear stress due to the fact that the discrepancies existing between the elastic stiffness coefficient ( $C_{66}$ ,  $C_{44}$ ,  $C_{55}$ ) of 'B' and 'F' is minimal when compared to the displacement or strains developed. In other words, the coupled displacements of BFB stacking sequence is more in contrast to FBF stacking sequence which results in higher stress value of BFB in spite of FBF stacking sequence having higher value of elastic stiffness. However, the maximum stresses are observed at the 'F' layer of both the stacking sequences. In addition, Figs. 6(g)-6(j) elucidate the significant effect of BFB and FBF stacking sequences on the electrical displacement and magnetic induction components, respectively. This can be due to the direct effect of electric and magnetic potential on these parameters.

Table 3 Effect of pyrocoupling associated with electro-magnetic boundary conditions on the maximum value of static parameters (SSSS;  $a=b=1$  m;  $h=0.3$  m)

Static Parameter (Max. value)	Stacking sequence	Open Circuit			Closed circuit		
		With pyroeffects	Without pyroeffects	% difference	With pyroeffects	Without pyroeffects	% difference
$\phi$ (V)	BFB	51.29	35.90	30.05	38.21	32.48	14.98
$D_x (\times 10^{-3} \text{ C/m}^2)$		6.95	5.57	19.86	4.4	3.69	16.17
$D_z (\times 10^{-3} \text{ C/m}^2)$		29.92	25.54	14.64	17.1	14.8	13.59
$\psi$ (A)	FBF	0.39	0.31	20.51	0.27	0.238	11.85
$B_x$ (Wb/m <sup>2</sup> )		0.22	0.172	21.92	0.16	0.132	17.43
$B_z$ (Wb/m <sup>2</sup> )		1.98	1.71	13.56	1.25	1.134	09.26

%difference=((with pyroeffects–without pyroeffects)/ with pyroeffects)×100

### 3.4 Effect of electro-magnetic boundary conditions

The influence of different electro-magnetic boundary conditions (Eq. (26)) on the coupled response of METE plates is evaluated. From Figs. 7 and 8, it can be witnessed that the open-circuit electro-magnetic boundary condition has a significant influence as opposed to that of the closed-circuit boundary condition. This may be attributed to the fact that the open circuit boundary condition facilitates a higher degree of coupling between the interacting fields. Further, the maximum values of static parameters accounting for different stacking sequence and electro-magnetic boundary conditions are illustrated in Table 2. From this table it is evident that the FBF-METE plate subjected to open-circuit boundary condition display higher magnitude of magnetic potential and magnetic flux density components. On the other hand, the BFB-METE plate with open-circuit boundary condition exhibit higher values of electric potential and electric displacement components.

### 3.5 Effect of $a/h$ ratio

The analysis is extended to evaluate the influence of aspect ratio ( $a/h$ ) on the static parameters of the METE plates, subjected to uniform temperature rise of 100 K. From Figs. 9(a)-9(f), it can be inferred that lower-aspect ratio has a significant influence on the static behaviour. This may be attributed to the fact that as the plate becomes thick, the effect of coupling increases. In this regard, the proposed FE formulation incorporating TSDT proves to be relevant in contrast to other kinematic displacement models.

### 3.6 Effect of pyrocoupling

This section addresses the effect of pyrocoupling on the static behaviour of METE plates through a comparison study. Since pyroelectric and pyromagnetic coupling has a predominant influence on potentials in contrast to other parameters, attention has been paid on the electric and magnetic potentials. From Figs. 10(a) and (b) it can be witnessed that as the temperature gradient increases the influence of pyrocoupling on the potentials drastically enhances. The reason is due to the fact that with higher temperature gradient, the magnitude of pyroelectric and pyromagnetic loads generated will be more. This in turn

leads to improved potentials. Further, from Figs. 11(a) and (b) it can be witnessed that the pyroeffects associated with open circuit conditions are predominant as opposed to closed circuit condition. The influence of pyrocoupling on the maximum values of potentials, electric displacements and magnetic flux densities of METE plates with different electro-magnetic boundary conditions are illustrated in Table 3. A similar inference with respect to pyrocoupling as that of Fig. 10 can be made here as well.

## 4. Conclusions

Numerical investigation on the static response of METE plates in the thermal environment is carried out through finite element approach. The coupled governing equations of motion are obtained via Hamilton's principle and in the framework of TSDT. The correctness of the present model is verified with the important previous researches. The significant numerical results of the present research suggest that TSDT improves the accuracy of predicting the static parameter of thick METE plates. Further, it is evident from the evaluation that a higher magnitude of temperature gradient results in enhanced value of the static parameters. In addition, the predominant influence of stacking sequence on the structural behaviours of METE plates is also noticed. A higher value of  $\phi$  and  $\psi$  is witnessed for BFB and FBF stacking sequences, respectively due to its higher electro-elastic and magneto-elastic coupling. In addition, it is witnessed that thick METE plates have a significant influence in contrast to thin plates. Meanwhile, investigation on the effect of various electro-magnetic boundary conditions reveals that open-circuit condition has a predominant effect as opposed to closed-circuit condition. Meanwhile, it is evident from the study that pyrocoupling also tends to influence the distribution of various static parameters across the plate thickness considerably. The results presented in the article may serve as benchmark solutions for optimum design and analysis of smart METE structures for sensors and actuators. It is believed that the results presented in this article will pave way for future sophisticated analysis of METE plates.

## Acknowledgement

The first author acknowledges the support of CV Raman Post-Doc fellowship by Indian Institute of Science (IISc), Bangalore under Institute of Eminence scheme.

## References

- Alaimo, A., Benedetti, I. and Milazzo, A. (2014), "A finite element formulation for large deflection of multilayered magneto-electro-elastic plates", *Compos. Struct.*, **107**, 643-653. <https://dx.doi.org/10.1016/j.compstruct.2013.08.032>.
- Altay, G. and Dokmeci, M.C. (2000), "Some Hamiltonian-type variational principles for motions of a hygro-thermoelastic medium", *J. Therm. Stress.*, **23**, 273-284. <https://doi.org/10.1080/014957300280443>.
- Ansari, R. and Gholmai, R. (2016), "Nonlocal free vibration in the pre- and postbuckled states of magneto-electro-thermo elastic rectangular nanoplates with various edge conditions", *Smart Mater. Struct.*, **25**, 095033.
- Badri, T.M. and Al-Kayiem, H.H. (2013), "Analytical solution for simply supported and multilayered Magneto-Electro-Elastic Plates", *Asian J. Scientif. Res.*, **6**, 236-244. <http://dx.doi.org/10.3923/ajsr.2013.236.244>.
- Benedetti, I. and Milazzo, A. (2017), "Advanced models for smart multilayered plates based on Reissner Mixed Variational Theorem", *Compos. Part B: Eng.*, **119**, 215-229. <http://dx.doi.org/10.1016%2Fj.compositesb.2017.03.007>.
- Chen, J., Chen, H., Pan, E. and Heyliger, P.R. (2007), "Modal analysis of magneto-electro-elastic plates using the state-vector approach", *J. Sound Vib.*, **304**(3), 722-734. <http://dx.doi.org/10.1016/j.jsv.2007.03.021>.
- Chen, W. and Shioya, T. (2001), "Piezothermoelastic behavior of a pyroelectric spherical shell", *J. Therm. Stress.*, **24**(2), 105-120. <https://doi.org/10.1080/01495730150500424>.
- Ebrahimi, F. and Barati, M.R. (2016b), "Hygrothermal buckling analysis of magnetically actuated embedded higher order functionally graded nanoscale beams considering the neutral surface position", *J. Therm. Stress.*, **39**(10), 1210-1229. <https://doi.org/10.1080/01495739.2016.1215726>.
- Ebrahimi, F. and Shafiei, N. (2017), "Influence of initial shear stress on the vibration behavior of single-layered graphene sheets embedded in an elastic medium based on Reddy's higher-order shear deformation plate theory", *Mech. Adv. Mater. Struct.*, **24**(9), 761-772. <https://doi.org/10.1080/15376494.2016.1196781>.
- Gholami, R., Ansari, R. and Gholami, Y. (2017), "Size-dependent bending, buckling and vibration of higher-order shear deformable magneto-electro-thermo-elastic rectangular nanoplates", *Mater. Res. Exp.*, **4**, 065702.
- Huang, D.J., Ding, H.J. and Chen, W.Q. (2007), "Analytical solution for functionally graded magneto-electro-elastic plane beams", *Int. J. Eng. Sci.*, **45**(2), 467-485. <https://doi.org/10.1016/j.ijengsci.2007.03.005>.
- Huang, D.J., Ding, H.J. and Chen, W.Q. (2010), "Static analysis of anisotropic functionally graded magneto-electro-elastic beams subjected to arbitrary loading", *Eur. J. Mech. A/Solid.*, **29**(3), 356-369. <https://doi.org/10.1016/j.euromechsol.2009.12.002>.
- Kattimani, S.C. and Ray, M.C. (2015), "Control of geometrically nonlinear vibrations of functionally graded magneto-electro-elastic plates", *Int. J. Mech. Sci.*, **99**, 154-167. <https://doi.org/10.1016/j.ijmecsci.2015.05.012>.
- Kerur, S.B. and Ghosh, A. (2013), "Geometrically non-linear bending analysis of piezoelectric fiber-reinforced composite (MFC/AFC) cross-ply plate under hygrothermal environment", *J. Therm. Stress.*, **36**(12), 1255-1282. <https://doi.org/10.1080/01495739.2013.818887>.
- Kondaiah, P., Shankar, K. and Ganesan, N. (2012), "Studies on magneto-electro-elastic cantilever beam under thermal environment", *Couple. Syst. Mech.*, **1**(2), 205-217. <http://dx.doi.org/10.12989/csm.2012.1.2.205>.
- Kondaiah, P., Shankar, K. and Ganesan, N. (2013a), "Pyroelectric and pyromagnetic effects on behaviour of magneto-electro-elastic plate", *Couple. Syst. Mech.*, **2**, 1-22. <https://doi.org/10.12989/csm.2013.2.1.001>.
- Kondaiah, P., Shankar, K. and Ganesan, N. (2013b), "Pyroelectric and pyromagnetic effects on multiphase magneto-electro-elastic cylindrical shells for axisymmetric temperature", *Smart Mater. Struct.*, **22**(2), 025007. <http://dx.doi.org/10.1088/0964-1726/22/2/025007>.
- Kumaravel, A., Ganesan, N. and Sethuraman, R. (2007), "Steady-state analysis of a three-layered electro-magneto-elastic strip in a thermal environment", *Smart Mater. Struct.*, **16**(2), 282-295. <https://doi.org/10.1088/0964-1726/16/2/006>.
- Lage, R.G., Soares, C.M.M., Soares, C.A.M. and Reddy, J.N. (2004), "Layerwise partial mixed finite element analysis of magneto-electro-elastic plates", *Comput. Struct.*, **82**(17), 1293-1301. <http://dx.doi.org/10.1016/j.compstruc.2004.03.026>.
- Milazzo, A. (2013), "A one-dimensional model for dynamic analysis of generally layered magneto-electro-elastic beams", *J. Sound Vib.*, **332**(2), 465-483. <http://dx.doi.org/10.1016/j.jsv.2012.09.004>.
- Milazzo, A. (2014a), "Layer-wise and equivalent single layer models for smart multilayered plates", *Compos. Part B: Eng.*, **67**, 62-75. <http://dx.doi.org/10.1016/j.compositesb.2014.06.021>.
- Milazzo, A. (2014b), "Refined equivalent single layer formulations and finite elements for smart laminates free vibrations", *Compos. Part B: Eng.*, **61**, 238-253. <http://dx.doi.org/10.1016/j.compositesb.2014.01.055>.
- Moita, J.M.S., Soares, C.M.M. and Soares, C.A.M. (2009), "Analyses of magneto-electro-elastic plates using a higher order finite element model", *Compos. Struct.*, **91**(4), 421-426. <http://dx.doi.org/10.1016/j.compstruct.2009.04.007>.
- Pan, E. (2001a), "Exact solution for simply supported and multilayered magneto-electro-elastic plates", *J. Appl. Mech.*, **68**(4), 608-618. <http://dx.doi.org/10.1115/1.1380385>.
- Pan, E. and Han, F. (2005), "Exact solution for functionally graded and layered magneto-electro-elastic plates", *Int. J. Eng. Sci.*, **43**(3), 321-339. <http://dx.doi.org/10.1016/j.ijengsci.2004.09.006>.
- Pan, E. and Heyliger, P.R. (2003), "Exact solutions for magneto-electro-elastic laminates in cylindrical bending", *Int. J. Solid. Struct.*, **40**(24), 6859-6876. <http://dx.doi.org/10.1016/j.ijsolstr.2003.08.003>.
- Razavi, S. and Shooshtari, A. (2015), "Nonlinear free vibration of magneto-electro-elastic rectangular plates", *Compos. Struct.*, **119**, 377-384. <https://doi.org/10.1016/j.compstruct.2014.08.034>.
- Reddy, J.N. (1997), *Mechanics of Laminated Composite Plates*, CRC Press, Boca Raton, FL, USA.
- Saadatfar, M. and Aghaie-Khafri, M. (2015), "On the behavior of a rotating functionally graded hybrid cylindrical shell with imperfect bonding subjected to hygrothermal condition", *J. Therm. Stress.*, **38**(8), 854-881. <https://doi.org/10.1080/01495739.2015.1038487>.
- Shooshtari, A. and Razavi, S. (2015a), "Large amplitude free vibration of symmetrically laminated magneto-electro-elastic rectangular plates on Pasternak type foundation", *Mech. Res. Commun.*, **69**, 103-113. <http://dx.doi.org/10.1016%2Fj.mechrescom.2015.06.011>.
- Shooshtari, A. and Razavi, S. (2015b), "Linear and nonlinear free vibration of a multilayered magneto-electro-elastic doubly-curved shell on elastic foundation", *Compos. Part B: Eng.*, **78**, 95-108. <http://dx.doi.org/10.1016%2Fj.compositesb.2015.03.070>.
- Shooshtari, A. and Razavi, S. (2016), "Large-amplitude free vibration of magneto-electro-elastic curved panels", *Scientia Iranica B*, **23**(6), 2606-2615.
- Sit, M., Ray, C. and Biswas, D. (2015), "Thermal stress analysis of laminated composite plates using third order shear deformation theory", *Advances in Structural Engineering*, Eds. Matsagar, V., Springer, New Delhi, 149-156.
- Sladek, J., Sladek, V., Krahulec, S. and Pan, E. (2013), "The MLPG analyses of large deflections of magneto-electroelastic

- plates", *Eng. Anal. Bound. Elem.*, **37**(4), 673-682. <https://doi.org/10.1016/j.enganabound.2013.02.001>.
- Sunar, M., Al-Garni, A.Z., Ali, M.H. and Kahraman, R. (2002), "Finite element modelling of thermopiezomagnetic smart structures", *ALAA J.*, **40**, 1845-1851. <https://doi.org/10.2514/2.1862>.
- Vinyas, M. (2019a), "A higher order free vibration analysis of carbon nanotube-reinforced magneto-electro-elastic plates using finite element methods", *Compos. Part B: Eng.*, **158**, 286-301. <https://doi.org/10.1016/j.compositesb.2018.09.086>.
- Vinyas, M. (2019b), "Vibration control of skew magneto-electro-elastic plates using active constrained layer damping", *Compos. Struct.*, **208**, 600-617. <https://doi.org/10.1016/j.compstruct.2018.10.046>.
- Vinyas, M. and Kattimani, S.C. (2017a), "Static studies of stepped functionally graded magneto-electro-elastic beam subjected to different thermal loads", *Compos. Struct.*, **163**, 216-237. <https://doi.org/10.1016/j.compstruct.2016.12.040>.
- Vinyas, M. and Kattimani, S.C. (2017b), "A Finite element based assessment of static behavior of multiphase magneto-electro-elastic beams under different thermal loading", *Struct. Eng. Mech.*, **62**(5), 519-535. <https://doi.org/10.12989/sem.2017.62.5.519>.
- Vinyas, M. and Kattimani, S.C. (2017c), "Static analysis of stepped functionally graded magneto-electro-elastic plates in thermal environment: A finite element study", *Compos. Struct.*, **178**, 63-85. <https://doi.org/10.1016/j.compstruct.2017.06.068>.
- Vinyas, M. and Kattimani, S.C. (2017d), "Static behavior of thermally loaded multilayered Magneto-Electro-Elastic beam", *Struct. Eng. Mech.*, **63**(4), 481-495. <https://doi.org/10.12989/sem.2017.63.4.41>.
- Vinyas, M. and Kattimani, S.C. (2017e), "Multiphysics response of magneto-electro-elastic beams in thermo-mechanical environment", *Coupl. Syst. Mech.*, **6**(3), 351-368. <https://doi.org/10.12989/csm.2017.6.3.351>.
- Vinyas, M. and Kattimani, S.C. (2017f), "A 3D finite element static and free vibration analysis of magneto-electro-elastic beam", *Coupl. Syst. Mech.*, **6**(4), 465-485. <https://doi.org/10.12989/csm.2017.6.4.465>.
- Vinyas, M. and Kattimani, S.C. (2017g), "Hygrothermal analysis of magneto-electro-elastic plate using 3D finite element analysis", *Compos. Struct.*, **180**, 617-637. <https://doi.org/10.1016/j.compstruct.2017.08.015>.
- Vinyas, M. and Kattimani, S.C. (2018a), "Finite element evaluation of free vibration characteristics of magneto-electro-elastic rectangular plates in hygrothermal environment using higher-order shear deformation theory", *Compos. Struct.*, **202**, 1339-1352. <https://doi.org/10.1016/j.compstruct.2018.06.069>.
- Vinyas, M. and Kattimani, S.C. (2018c), "Investigation of the effect of BaTiO<sub>3</sub>/CoFe<sub>2</sub>O<sub>4</sub> particle arrangement on the static response of magneto-electro-thermo-elastic plates", *Compos. Struct.*, **185**, 51-64. <https://doi.org/10.1016/j.compstruct.2017.10.073>.
- Vinyas, M. and Kattimani, S.C. (2019a), "Finite element simulation of controlled frequency response of skewed multiphase magneto-electro-elastic plates", *J. Intel. Mater. Syst. Struct.*, **30**(12), 1757-1771. <https://doi.org/10.1177/1045389X19843674>.
- Vinyas, M., Kattimani, S.C. and Sharanappa, J. (2018b), "Hygrothermal coupling analysis of magneto-electro-elastic beams using finite element methods", *J. Therm. Stress.*, **41**(8), 1063-1079. <https://doi.org/10.1080/01495739.2018.1447856>.
- Vinyas, M., Kattimani, S.C., Harursampath, D. and Nguyen Thoi, T. (2019c), "Coupled evaluation of the free vibration characteristics of magneto-electro-elastic skew plates in hygrothermal environment", *Smart Struct. Syst.*, **24**(2), 267-292. <https://doi.org/10.12989/ss.2019.24.2.267>.
- Vinyas, M., Kattimani, S.C., Loja, M.A.R. and Vishwas, M. (2018), "Effect of BaTiO<sub>3</sub>/CoFe<sub>2</sub>O<sub>4</sub> micro-topological textures on the coupled static behaviour of magneto-electro-thermo-elastic beams indifferent thermal environment", *Mater. Res. Exp.*, **5**, 125702. <https://doi.org/10.1088/2053-1591/aae0c8>.
- Vinyas, M., Nischith, G., Loja, M.A.R., Ebrahimi, F. and Duc, N.D. (2019a), "Numerical analysis of the vibration response of skew magneto-electro-elastic plates based on the higher-order shear deformation theory", *Compos. Struct.*, **214**, 132-142. <https://doi.org/10.1016/j.compstruct.2019.02.010>.
- Vinyas, M., Piyush, J.S. and Kattimani, S.C. (2017a), "Influence of coupled fields on free vibration and static behavior of functionally graded magneto-electro-thermo-elastic plate", *J. Intel. Mater. Syst. Struct.*, **29**(7), 1430-1455. <https://doi.org/10.1177/1045389X17740739>.
- Vinyas, M., Sandeep, A.S., Trung, N.T., Ebrahimi, F. and Duc, N.D. (2019d), "A finite element based assessment of free vibration behaviour of circular and annular magneto-electro-elastic plates using higher order shear deformation theory", *J. Intel. Mater. Syst. Struct.*, **30**(6), 2478-2501. <https://doi.org/10.1177/1045389X19862386>.
- Vinyas, M., Sunny, K.K., Harursampath, D., Trung, N.T. and Loja, M.A.R. (2019b), "Influence of interphase on the multi-physics coupled frequency of three phase smart magneto-electro-elastic composite plates", *Compos. Struct.*, **226**, 111254. <https://doi.org/10.1016/j.compstruct.2019.111254>.
- Wang, J., Chen, L. and Fang, S. (2003), "State vector approach to analysis of multilayered magneto-electro-elastic plates", *Int. J. Solid. Struct.*, **40**(7), 1669-1680. [https://doi.org/10.1016/S0020-7683\(03\)00027-1](https://doi.org/10.1016/S0020-7683(03)00027-1).
- Xin, L. and Hu, Z. (2015), "Free vibration of simply supported and multilayered magneto-electro-elastic plates", *Compos. Struct.*, **121**, 344-350. <https://doi.org/10.1016/j.compstruct.2014.11.030>.

CC

## Appendix A

The different material properties appearing in Eqs. (1)-(3) can be encapsulated as follows:

$[C^n]$	Elastic stiffness matrix
$\{D^n\}$	Electric displacement vector
$[e^n]$	Piezoelectric coefficient matrix
$\{E^n\}$	Electric field vector
$[m^n]$	Electromagnetic coefficient matrix
$\{p^n\}$	Pyroelectric coefficient vector
$[q^n]$	Magnetostrictive coefficient matrix
$\{\sigma^n\}$	Stress tensor
$[\alpha^n]$	thermal expansion coefficient matrix
$\{\varepsilon^n\}$	Strain tensor of the $n^{\text{th}}$ layer
$[\eta^n]$	Dielectric constant matrix
$[\lambda^n]$	Pyromagnetic coefficient vector
$[\mu^n]$	Magnetic permeability constant matrix
$\{B^n\}$	Magnetic flux density matrix

## Transformations from Natural coordinate $(\xi, \eta)$ to Cartesian coordinate $(x, y)$

The governing equations of motion to predict the static parameters of METE plate can be obtained once the derivative of shape functions matrices are established in Cartesian coordinate  $(x, y)$ . Since, the shape functions depicted in Eq. (13) corresponds to the natural coordinates  $(\xi, \eta)$ , it is required to transform it to Cartesian coordinate using Jacobian Matrix  $[J]$  as follows

$$\begin{Bmatrix} \frac{\partial N_i}{\partial x} \\ \frac{\partial N_i}{\partial y} \end{Bmatrix} = \begin{bmatrix} \frac{\partial \xi}{\partial x} & \frac{\partial \eta}{\partial x} \\ \frac{\partial \xi}{\partial y} & \frac{\partial \eta}{\partial y} \end{bmatrix} \begin{Bmatrix} \frac{\partial N_i}{\partial \xi} \\ \frac{\partial N_i}{\partial \eta} \end{Bmatrix} = [J]^{-1} \begin{Bmatrix} \frac{\partial N_i}{\partial \xi} \\ \frac{\partial N_i}{\partial \eta} \end{Bmatrix} \quad (\text{A-1})$$

where,  $[J]^{-1}$  is the inverse of Jacobian matrix. It can also be established that

$$dxdy = |J|d\xi d\eta \quad (\text{A-2})$$

in which,  $|J|$  is the determinant of Jacobian matrix.

Now, the different derivative of shape function matrices such as  $[B_{tbi}]$ ,  $[B_{rbi}]$ ,  $[B_{tsi}]$  illustrated in Eq. (19) are obtained using Eq. (A-1) as follows

$$\begin{aligned} [B_{tbi}] &= \begin{bmatrix} \frac{\partial N_i}{\partial x} & 0 & 0 \\ 0 & \frac{\partial N_i}{\partial y} & 0 \\ \frac{\partial N_i}{\partial y} & \frac{\partial N_i}{\partial x} & 0 \end{bmatrix} = [J]^{-1} \begin{bmatrix} \frac{\partial N_i}{\partial \xi} & 0 & 0 \\ 0 & \frac{\partial N_i}{\partial \eta} & 0 \\ \frac{\partial N_i}{\partial \eta} & \frac{\partial N_i}{\partial \xi} & 0 \end{bmatrix}; \\ [B_{rbi}] &= \begin{bmatrix} \frac{\partial N_i}{\partial x} & 0 \\ 0 & \frac{\partial N_i}{\partial y} \\ \frac{\partial N_i}{\partial y} & \frac{\partial N_i}{\partial x} \end{bmatrix} = [J]^{-1} \begin{bmatrix} \frac{\partial N_i}{\partial \xi} & 0 \\ 0 & \frac{\partial N_i}{\partial \eta} \\ \frac{\partial N_i}{\partial \eta} & \frac{\partial N_i}{\partial \xi} \end{bmatrix}; \\ [B_{tsi}] &= \begin{bmatrix} 0 & 0 & \frac{\partial N_i}{\partial x} \\ 0 & 0 & \frac{\partial N_i}{\partial y} \end{bmatrix} = [J]^{-1} \begin{bmatrix} 0 & 0 & \frac{\partial N_i}{\partial \xi} \\ 0 & 0 & \frac{\partial N_i}{\partial \eta} \end{bmatrix} \quad (\text{A-3}) \end{aligned}$$

The derivative of shape function matrices transformed to

Cartesian coordinates (Eq. (A-3)) are then used to establish the strain relationships (Eq. (16)) which later incorporated in Eq. (22) to represent the Hamilton's principle in the Cartesian coordinates.

## Appendix B

The different stiffness matrices and force vectors used in this study are transformed from natural coordinates to Cartesian coordinates using Eqs. (A-1) to (A-3). The general form can be represented as follows

$$\begin{aligned} [K^e] &= \int_0^b \int_0^a [B]^T [D] [B] dxdy \\ &= \int_{-1}^1 \int_{-1}^1 [B(\xi, \eta)]^T [D] [B(\xi, \eta)] |J(\xi, \eta)| d\xi d\eta \\ [F^e] &= \int_0^b \int_0^a [B]^T [D] dxdy \\ &= \int_{-1}^1 \int_{-1}^1 [B(\xi, \eta)]^T [D] |J(\xi, \eta)| d\xi d\eta \quad (\text{B-1}) \end{aligned}$$

The explicit representation of the stiffness matrices (in Cartesian coordinates) appearing in the Eq. (24) can be shown as follows

$$\begin{aligned} [K_{tt}^e] &= [K_{tbb1}^e] + [K_{ts1}^e], [K_{tr}^e] = [K_{rtb24}^e]^T + [K_{rts13}^e]^T \\ [K_{tr}^e] &= [K_{rtb4}^e]^T + [K_{rts3}^e]^T, \\ [K_{t\phi}^e] &= [K_{tb\phi1}^e] + [K_{ts\phi1}^e], \\ [K_{t\psi}^e] &= [K_{tb\psi1}^e] + [K_{ts\psi1}^e], \\ [K_{rr}^e] &= [K_{rrb5735}^e] + [K_{rrs3513}^e], \\ [K_{rr*}^e] &= [K_{rrb57}^e] + [K_{rrs35}^e], \\ [K_{r\phi}^e] &= [K_{rb\phi24}^e] + [K_{r\phi s13}^e], \\ [K_{r\psi}^e] &= [K_{rb\psi24}^e] + [K_{r\psi s13}^e], \\ [K_{r**}^e] &= [K_{rrb7}^e] + [K_{rrs5}^e], \\ [K_{r*\phi}^e] &= [K_{rb\phi4}^e] + [K_{r\phi s3}^e], \\ [K_{r*\psi}^e] &= [K_{rb\psi4}^e] + [K_{r\psi s3}^e], \\ [K_{rrt}^e] &= [K_{rtb24}^e] + [K_{rts13}^e], \\ [K_{rrb5735}^e] &= [K_{rrb57}^e] + [K_{rrb35}^e], \\ [K_{rrs3513}^e] &= [K_{rrs35}^e] + [K_{rrs13}^e], \\ [K_{rrb57}^e] &= [K_{rrb5}^e] + [K_{rrb7}^e], \\ [K_{rrb35}^e] &= [K_{rrb3}^e] + [K_{rrb5}^e], \\ [K_{rrs35}^e] &= [K_{rrs3}^e] + [K_{rrs5}^e], \\ [K_{rrs13}^e] &= [K_{rrs1}^e] + [K_{rrs3}^e], \\ [K_{rb\phi24}^e] &= [K_{rb\phi2}^e] + [K_{rb\phi4}^e], \\ [K_{r\phi s13}^e] &= [K_{r\phi s1}^e] + [K_{r\phi s3}^e], \end{aligned}$$



$$\begin{aligned} [K_{rb\psi 24}^e] &= [K_{rb\psi 2}^e] + [K_{rb\psi 4}^e], \\ [K_{r\psi s13}^e] &= [K_{r\psi s1}^e] + [K_{r\psi s3}^e] \end{aligned} \quad (B-2)$$

where

$$\begin{aligned} [K_{\psi\psi}^e] &= \int_0^a \int_0^b [B_{\psi}]^T [D_{\psi\psi}] [B_{\psi}] dx dy, \\ [K_{\phi\phi}^e] &= \int_0^a \int_0^b [B_{\phi}]^T [D_{\phi\phi}] [B_{\phi}] dx dy, \\ [K_{tb1}^e] &= \int_0^a \int_0^b [B_{tb}]^T [D_{b1}] [B_{tb}] dx dy, \\ [K_{ts1}] &= \int_0^a \int_0^b [B_{ts}]^T [D_{s1}] [B_{ts}] dx dy, \\ [K_{rb4}^e] &= \int_0^a \int_0^b [B_{rb}]^T [D_{b4}] [B_{rb}] dx dy, \\ [K_{rs3}^e] &= \int_0^a \int_0^b [B_{rs}]^T [D_{s3}] [B_{rs}] dx dy, \\ [K_{tb\phi1}^e] &= \int_0^a \int_0^b [B_{tb}]^T [D_{b\phi1}] [B_{\phi}] dx dy, \\ [K_{ts\phi1}^e] &= \int_0^a \int_0^b [B_{ts}]^T [D_{s\phi1}] [B_{\phi}] dx dy, \\ [K_{tb\psi1}^e] &= \int_0^a \int_0^b [B_{tb}]^T [D_{b\psi1}] [B_{\psi}] dx dy, \\ [K_{ts\psi1}^e] &= \int_0^a \int_0^b [B_{ts}]^T [D_{s\psi1}] [B_{\psi}] dx dy, \\ [K_{rb7}^e] &= \int_0^a \int_0^b [B_{rb}]^T [D_{b7}] [B_{rb}] dx dy, \\ [K_{rs5}^e] &= \int_0^a \int_0^b [B_{rs}]^T [D_{s5}] [B_{rs}] dx dy, \\ [K_{rb\phi4}^e] &= \int_0^a \int_0^b [B_{rb}]^T [D_{b\phi4}] [B_{\phi}] dx dy, \\ [K_{r\phi s3}^e] &= \int_0^a \int_0^b [B_{rs}]^T [D_{s\phi3}] [B_{\phi}] dx dy, \\ [K_{rb\psi4}^e] &= \int_0^a \int_0^b [B_{rb}]^T [D_{b\psi4}] [B_{\psi}] dx dy, \\ [K_{r\psi s3}^e] &= \int_0^a \int_0^b [B_{rs}]^T [D_{s\psi3}] [B_{\psi}] dx dy, \\ [K_{rrb5}^e] &= \int_0^a \int_0^b [B_{rb}]^T [D_{b5}] [B_{rb}] dx dy, \\ [K_{rrb7}^e] &= \int_0^a \int_0^b [B_{rb}]^T [D_{b7}] [B_{rb}] dx dy, \\ [K_{rrb3}^e] &= \int_0^a \int_0^b [B_{rb}]^T [D_{b3}] [B_{rb}] dx dy, \end{aligned}$$

$$\begin{aligned} [K_{rrs1}^e] &= \int_0^a \int_0^b [B_{rs}]^T [D_{s1}] [B_{rs}] dx dy, \\ [K_{rrs3}^e] &= \int_0^a \int_0^b [B_{rs}]^T [D_{s3}] [B_{rs}] dx dy, \\ [K_{rrs5}^e] &= \int_0^a \int_0^b [B_{rs}]^T [D_{s5}] [B_{rs}] dx dy, \\ [K_{rb\phi2}^e] &= \int_0^a \int_0^b [B_{rb}]^T [D_{b\phi2}] [B_{\phi}] dx dy, \\ [K_{rb\phi4}^e] &= \int_0^a \int_0^b [B_{rb}]^T [D_{b\phi4}] [B_{\phi}] dx dy, \\ [K_{rb\psi2}^e] &= \int_0^a \int_0^b [B_{rb}]^T [D_{b\psi2}] [B_{\psi}] dx dy, \\ [K_{rb\psi4}^e] &= \int_0^a \int_0^b [B_{rb}]^T [D_{b\psi4}] [B_{\psi}] dx dy, \\ [K_{r\phi s1}^e] &= \int_0^a \int_0^b [B_{rs}]^T [D_{s\phi1}] [B_{\phi}] dx dy, \\ [K_{r\phi s3}^e] &= \int_0^a \int_0^b [B_{rs}]^T [D_{s\phi3}] [B_{\phi}] dx dy, \\ [K_{r\psi s1}^e] &= \int_0^a \int_0^b [B_{rs}]^T [D_{s\psi1}] [B_{\psi}] dx dy, \\ [K_{r\psi s3}^e] &= \int_0^a \int_0^b [B_{rs}]^T [D_{s\psi3}] [B_{\psi}] dx dy, \\ [K_{rs1}^e] &= \int_0^a \int_0^b [B_{rs}]^T [D_{s1}] [B_{ts}] dx dy, \\ [K_{rs3}^e] &= \int_0^a \int_0^b [B_{rs}]^T [D_{s3}] [B_{ts}] dx dy, \\ [K_{rb2}^e] &= \int_0^a \int_0^b [B_{rb}]^T [D_{b2}] [B_{tb}] dx dy, \\ [F_{\Delta Trb4}^e] &= \int_0^a \int_0^b [B_{rb}]^T [D_{th4}] dx dy, \\ [F_{\Delta Trb2}^e] &= \int_0^a \int_0^b [B_{rb}]^T [D_{th2}] dx dy, \\ [F_{\Delta Trb1}^e] &= \int_0^a \int_0^b [B_{tb}]^T [D_{th1}] dx dy, \\ [F_{\Delta Trb24}^e] &= [F_{\Delta Trb2}^e] + [F_{\Delta Trb4}^e], \\ [F_{\phi-\Delta T}^e] &= \int_0^a \int_0^b [B_{\phi}]^T [D_{\phi-\Delta T}] dx dy, \\ [F_{\psi-\Delta T}^e] &= \int_0^a \int_0^b [B_{\psi}]^T [D_{\psi-\Delta T}] dx dy, \end{aligned} \quad (B-3)$$

The various rigidity matrices contributing to Eq. (B-3) can be denoted as follows

$$[D_{b1}] = \sum_{n=1}^N \int_{h_n}^{h_{n+1}} [C_b]^n dz, [D_{b2}] = \sum_{n=1}^N \int_{h_n}^{h_{n+1}} z [C_b]^n dz,$$

$$\begin{aligned}
[D_{b3}] &= \sum_{n=1}^N \int_{h_n}^{h_{n+1}} z^2 [C_b]^n dz, \quad [D_{b4}] = \sum_{n=1}^N \int_{h_n}^{h_{n+1}} c_1 z^3 [C_b]^n dz, \\
[D_{b5}] &= \sum_{n=1}^N \int_{h_n}^{h_{n+1}} c_1 z^4 [C_b]^n dz, \quad [D_{b7}] = \sum_{n=1}^N \int_{h_n}^{h_{n+1}} c_1^2 z^6 [C_b]^n dz \\
[D_{b\phi 1}] &= \sum_{n=1}^N \int_{h_n}^{h_{n+1}} [e_b]^n dz, \quad [D_{b\phi 2}] = \sum_{n=1}^N \int_{h_n}^{h_{n+1}} z [e_b]^n dz, \\
[D_{b\phi 4}] &= \sum_{n=1}^N \int_{h_n}^{h_{n+1}} c_1 z^3 [e_b]^n dz, \quad [D_{b\psi 1}] = \sum_{n=1}^N \int_{h_n}^{h_{n+1}} [q_b]^n dz, \\
[D_{b\psi 2}] &= \sum_{n=1}^N \int_{h_n}^{h_{n+1}} z [q_b]^n dz, \quad [D_{b\psi 4}] = \sum_{n=1}^N \int_{h_n}^{h_{n+1}} c_1 z^3 [q_b]^n dz \\
[D_{s1}] &= \sum_{n=1}^N \int_{h_n}^{h_{n+1}} [C_s]^n dz, \quad [D_{s3}] = \sum_{n=1}^N \int_{h_n}^{h_{n+1}} c_2 z^2 [C_s]^n dz, \\
[D_{s5}] &= \sum_{n=1}^N \int_{h_n}^{h_{n+1}} c_2^2 z^4 [C_s]^n dz, \quad [D_{s\phi 1}] = \sum_{n=1}^N \int_{h_n}^{h_{n+1}} [e_s]^n dz, \\
[D_{s\phi 3}] &= \sum_{n=1}^N \int_{h_n}^{h_{n+1}} c_2 z^2 [e_s]^n dz, \quad [D_{s\psi 1}] = \sum_{n=1}^N \int_{h_n}^{h_{n+1}} [q_s]^n dz, \\
[D_{s\psi 3}] &= \sum_{n=1}^N \int_{h_n}^{h_{n+1}} c_2 z^2 [q_s]^n dz, \\
[D_{\phi\phi}] &= \sum_{n=1}^N \int_{h_n}^{h_{n+1}} [\eta]^n dz, \quad [D_{\psi\psi}] = \sum_{n=1}^N \int_{h_n}^{h_{n+1}} [\mu]^n dz, \\
[D_{\phi\psi}] &= \sum_{n=1}^N \int_{h_n}^{h_{n+1}} [m]^n dz, \\
[D_{th4}] &= \sum_{n=1}^N \int_{h_n}^{h_{n+1}} c_1 z^3 [C_b]^n [\alpha]^n \Delta T dz, \\
[D_{th2}] &= \sum_{n=1}^N \int_{h_n}^{h_{n+1}} z [C_b]^n [\alpha]^n \Delta T dz, \\
[D_{th1}] &= \sum_{n=1}^N \int_{h_n}^{h_{n+1}} [C_b]^n [\alpha]^n \Delta T dz, \\
[D_{\phi-\Delta T}] &= \sum_{n=1}^N \int_{h_n}^{h_{n+1}} [p]^n \Delta T dz, \\
[D_{\psi-\Delta T}] &= \sum_{n=1}^N \int_{h_n}^{h_{n+1}} [\lambda]^n \Delta T dz
\end{aligned} \tag{B-4}$$